

## GALAXY CLUSTERS IN HUBBLE VOLUME SIMULATIONS: COSMOLOGICAL CONSTRAINTS FROM SKY SURVEY POPULATIONS

A.E. EVRARD<sup>1</sup>, T.J. MACFARLAND<sup>2,3</sup>, H.M.P. COUCHMAN<sup>4</sup>, J.M. COLBERG<sup>5,6</sup>, N. YOSHIDA<sup>5</sup>,  
S.D.M. WHITE<sup>5</sup>, A.R. JENKINS<sup>7</sup>, C.S. FRENK<sup>7</sup>, F.R. PEARCE<sup>7</sup>, G. EFSTATHIOU<sup>8</sup>, J.A.  
PEACOCK<sup>9</sup>, P.A. THOMAS<sup>10</sup> (*The Virgo Consortium*)

<sup>1</sup>Departments of Physics and Astronomy, University of Michigan, Ann Arbor, MI 48109-1120 USA

<sup>2</sup>Rechenzentrum Garching, Boltzmannstr. 2, D-85740 Garching, Germany

<sup>4</sup>Dept of Physics and Astronomy, McMaster University, Hamilton, Ontario, L8S 4M1, Canada

<sup>5</sup>Max-Planck-Institut für Astrophysik, Karl-Schwarzschild-Str. 1, D-85740 Garching, Germany

<sup>7</sup>Dept. of Physics, Durham University, South Road, Durham DH1 3LE, UK

<sup>8</sup>Institute of Astronomy, Madingley Road, Cambridge CB3 0HA, UK

<sup>9</sup>Institute for Astronomy, University of Edinburgh, Royal Observatory, Edinburgh EH9 3HJ, UK

<sup>10</sup>Astronomy Centre, CEPS, University of Sussex, Brighton BN1 9QJ, UK

*DRAFT, submitted to ApJ 10 October 2001*

### ABSTRACT

We use giga-particle N-body simulations to study galaxy cluster populations in Hubble Volumes of  $\Lambda$ CDM ( $\Omega_m = 0.3$ ,  $\Omega_\Lambda = 0.7$ ) and  $\tau$ CDM ( $\Omega_m = 1$ ) world models. Mapping past light-cones of locations in the computational space, we create mock sky surveys of dark matter structure to  $z \simeq 1.4$  over 10,000 sq deg and to  $z \simeq 0.5$  over two full spheres. Calibrating the Jenkins mass function at  $z=0$  with samples of  $\sim 1.5$  million clusters, we show that the fit describes the sky survey counts to  $\lesssim 20\%$  accuracy over all redshifts for systems more massive than poor galaxy groups ( $5 \times 10^{13} h^{-1} M_\odot$ ). We examine cosmic variance in the number density of local cluster samples and find it to roughly double the squared error in the power spectrum normalization  $\sigma_8$  derived from current data.

Using dark matter velocity dispersion as an indicator of X-ray temperature, we compare the behavior of high redshift cluster counts to EMSS and RDCS X-ray selected surveys. The  $\Lambda$ CDM model matches the observations under economical assumptions for ICM evolution, while  $\tau$ CDM can be made consistent under non-standard assumptions that are not yet formally ruled out. Upcoming SZ search counts are very sensitive to  $\sigma_8$  uncertainty but we demonstrate, using transformations of the discrete cluster samples that mimic variation in  $\sigma_8$ , that the median redshift of clusters above  $10^{14} h^{-1} M_\odot$  in a single 10 sq deg field can discriminate between the two cosmologies at a minimum of 95% confidence.

For  $\Lambda$ CDM, the characteristic temperature at fixed sky surface density is a weak function of redshift, implying an abundance of hot clusters at  $z > 1$ . In the Sloan Survey area, one 8 keV cluster at  $z > 2$  and ten 5 keV clusters at  $z > 3$  are expected for  $\sigma_8 \simeq 0.9$ . Too many such clusters can falsify the model; detection of Coma-sized clusters at  $z > 1$  violate  $\Lambda$ CDM at 95% confidence if their surface density exceeds 0.003 per sq deg, or 120 on the whole sky.

*Subject headings:* cosmology:theory — dark matter — gravitation; clusters: general — intergalactic medium — cosmology

### 1. INTRODUCTION

Studies of galaxy clusters provide a critical interface between cosmological structure formation and the astrophysics of galaxy formation. Spatial statistics of the cluster population provide valuable constraints on cosmological parameters while multi-wavelength studies of cluster content offer insights into the cosmic mix of matter components and into the interactions between galaxies and their local environments.

In the near future, the size and quality of observed cluster samples will grow dramatically as surveys in optical, X-ray and sub-mm wavelengths are realized. In the optical, the ongoing wide field 2dF (Colless *et al.* 2001) and SDSS (Kepner *et al.* 1999; Nichol *et al.* 2001; Annis *et al.*

2001) surveys will map the galaxy and cluster distributions over large fractions of the sky to moderate ( $z \sim 0.3$ ) depth, while deeper surveys are probing of order tens of degrees of sky to  $z \sim 1$  (Postman *et al.* 1996; Dalton *et al.* 1997; Zaritsky *et al.* 1997; Ostrander *et al.* 1998; Scoddeggio *et al.* 1999; Gal *et al.* 2000; Gladders & Yee 2000; Willlick *et al.* 2001; Gonzalez *et al.* 2001). In the X-ray, ROSAT archival surveys (Scharf *et al.* 1997; Rosati *et al.* 1998; Ebeling *et al.* 1998; Viklinin *et al.* 1998; deGrandi *et al.* 1999; Bohringer *et al.* 2001; Ebeling, Edge & Henry 2001; Gioia *et al.* 2001) have generated redshift samples of many hundreds of clusters. Similar surveys to come from developing Chandra and XMM archives (*e.g.*, Romer *et al.* 2001) will lead to order of magnitude improvements

<sup>3</sup>1Click Brands LLC, 704 Broadway, New York, NY 10003, USA

<sup>6</sup>Econovo Software, 1 State Street, Boston MA 02109 USA

in sample size and limiting sensitivity. Finally, the detection of clusters via their spectral imprint on the microwave background (Sunyaev & Zel'dovich 1972; Birkinshaw 1999) offers a new mode of efficiently surveying for very distant ( $z > 1$ ) clusters with hot, intracluster plasma (Barbosa *et al.* 1996; Holder *et al.* 2000; Kneissl *et al.* 2001).

Deciphering the cosmological and astrophysical information in the coming era of large survey data sets requires the ability to accurately compute expectations for observables. Given some survey observation  $\mathcal{R}$  at redshift  $z$ , a likelihood analysis requires the probability  $p(\mathcal{R}|z, \mathcal{C}, \mathcal{A})$  that such data would arise within a model described by sets of cosmological  $\mathcal{C} \equiv \{C_i\}$  and astrophysical  $\mathcal{A} \equiv \{A_j\}$  parameters. Since it is natural to use total mass  $M$  as the independent variable ordering the cluster population, this likelihood can be considered to be a product

$$p(\mathcal{R}|z, \mathcal{C}, \mathcal{A}) = p(M|z, \mathcal{C}) p(\mathcal{R}|M, z, \mathcal{A}) \quad (1)$$

of the likelihood  $p(M|z, \mathcal{C})$  that a cluster of mass  $M$  exists in the survey of interest at redshift  $z$  in cosmology  $\mathcal{C}$  and the likelihood  $p(\mathcal{R}|M, z, \mathcal{A})$  that observable  $\mathcal{R}$  is associated with such a cluster given the astrophysical model  $\mathcal{A}$ .

A measure that has been the subject of extensive study is the probability of finding a cluster at redshift  $z$  with total mass  $M$  or larger in a comoving volume element  $dV$

$$p(>M, z | \mathcal{C}) \propto n(>M, z | \mathcal{C}) dV \quad (2)$$

where  $n(>M, z | \mathcal{C})$  is the cumulative comoving space density of clusters at redshift  $z$ . The absence of explicit astrophysical dependence in equation (2) reflects the assumption that weakly interacting dark matter dominates the matter energy density; the total mass  $M$  is relatively immune to astrophysical processes. The  $p(\mathcal{R}|M, z, \mathcal{A})$  term, on the other hand, is often critically dependent on the astrophysical model. For optical and X-ray observations, it incorporates the answer to the difficult question “How do dark matter potential wells light up?”

For the case of Gaussian initial fluctuation spectra, Press & Schechter (1974; PS) used a spherical collapse argument and  $N$ -body simulation to show that the differential space density, the *mass function*  $n(M, z) d \ln M$ , of the rarest clusters is exponentially sensitive to the amplitude of density perturbations on  $\sim 10 h^{-1}$  Mpc scales. The analytic form of PS was put on a more rigorous footing by Bond *et al.* (1991), but recent extensions to ellipsoidal collapse (Sheth & Tormen 1999; Lee & Shandarin 1999) result in modifications of the original functional form. Calibration by N-body simulations has led to a functional shape for the mass function that retains the essential character of the original PS derivation (Jenkins *et al.* 2001, hereafter J01, and references therein). For cluster masses defined using threshold algorithms tied to the cosmic mean mass density  $\bar{\rho}_m(z)$ , J01 show that the mass fraction in collapsed objects is well described by a single function that depends only on the shape of the filtered power spectrum of initial fluctuations  $\sigma^2(M)$ .

Complications arise in determining the mass function  $n(M, z)$  from both simulations and observations. The first is semantic. Clusters formed from hierarchical clustering in three dimensions do not possess distinct or even unique physical boundaries. The mass of a cluster depends on the

spatial region used to define it. This complication is solvable by convention. We choose here a commonly employed measure  $M_\Delta$  defined as the mass within a spherical region, centered on a local density maximum, whose mean interior density is a fixed multiple  $\Delta$  of the critical density  $\rho_c(z)$  at the epoch of interest  $z$ . Acknowledging the non-unique choice of threshold  $\Delta$ , we develop in an appendix a model, based on the mean density profile of clusters derived from simulations (Navarro, Frenk & White 1996; 1997), that transforms the mass function fit parameters to threshold values different from that used here.

Attempts to empirically constrain the mass function are complicated by the fact that it is not possible to directly observe the theoretically defined mass  $M_\Delta$ . Instead, a surrogate estimator  $\mathcal{M}$  must be employed that is, in general, a biased and noisy representation of  $M_\Delta$ . For example, estimates derived from the weak gravitational lensing distortions induced on background galaxies are likely to overestimate the true mass by  $\sim 30\%$ , with a dispersion of similar magnitude (Metzler, White & Loken 2001). An additional complication in computing  $n(M, z)$  from deep cluster counts is that the redshift space volume element  $dV \equiv \frac{dV}{dz}(z | \mathcal{C}) dz$  requires knowledge of the underlying cosmological model.

The temperature  $T$  of the intracluster medium (ICM) derived from X-ray spectroscopy is an observationally accessible mass estimator. Gas dynamic simulations predict that the ICM rarely strays far from virial equilibrium (Evrard 1990; Evrard, Metzler & Navarro 1996; Bryan & Norman 1998; Yoshikawa, Jing & Suto 2000; Mathiesen & Evrard 2001), so that  $p(M | T)$  is well described by a mean power-law relation with narrow ( $\lesssim 15\%$  in mass) intrinsic scatter. Observations are generally supportive of this picture (Hjorth, Oukbir & van Kampen 1998; Mohr, Mathiesen & Evrard 1999; Horner *et al.* 1999; Nevalainen *et al.* 2000), but the detailed form of  $p(M | T)$  remains uncertain. The overall normalization is a particular concern; we cannot prove that we know the median mass of, say, a 6 keV cluster to better than 20% accuracy.

Even with this degree of uncertainty, the space density of clusters as a function of  $T$  (the *temperature function*) has been used to place tight constraints on  $\sigma_8$ , the present, linear-evolved amplitude of density fluctuations averaged within spheres of radius  $8 h^{-1}$  Mpc. Henry & Arnaud (1991) derived  $\sigma_8 = 0.59 \pm 0.02$  from temperatures of 25 clusters in a bright, X-ray flux limited sample, assuming  $\Omega_m = 1$ . Subsequent analysis of this sample (White, Efstathiou & Frenk 1993; Eke, Cole & Frenk 1996; Vianna & Liddle 1996; Fan, Bahcall & Cen 1997; Kitayama & Suto 1997; Pen 1998) and revised samples (Markevitch 1998; Blanchard *et al.* 2000) generated largely consistent results and extended constraints to arbitrary  $\Omega_m$ . For example, Pierpaoli, Scott & White (2001), reanalyzing the Markevitch sample using revised temperatures of White (2000), find

$$\sigma_8 = 0.495^{+0.034}_{-0.037} \Omega_m^{-0.60}. \quad (3)$$

The 7% fractional error is typical of the uncertainties quoted by previous studies.

Accurate determination of  $\sigma_8$  is a prerequisite for deriving constraints on the clustered mass density  $\Omega_m$  from a differential measurement of the local and high redshift cluster spatial abundances. Most studies have excluded

the possibility that  $\Omega_m = 1$  from current data (Luppino & Kaiser 1997; Bahcall, Fan & Cen 1997; Carlberg, Yee & Ellingson 1997; Donahue *et al.* 1998; Eke *et al.* 1998; Bahcall & Fan 1998) but others disagree (Sadat, Blanchard & Oukbir 1998; Blanchard & Barlett 1998; Vianna & Liddle 1999). Uncertainty in  $\sigma_8$  plays a role in this ambiguity, as recently illustrated by Borgani *et al.* (1999a). In their analysis of 16 CNO clusters at redshifts  $0.17 \leq z \leq 0.55$ , the estimated value of  $\Omega_m$  shifts by a factor 3, from 0.35 to 1.05, as  $\sigma_8$  is varied from 0.5 to 0.6.

Motivated by the need to study systematic effects in both local and distant cluster samples, we investigate the spatial distribution of clusters in real and redshift space samples derived from  $N$ -body simulations of cosmic volumes comparable in scale to the Hubble Volume ( $c/H_0$ )<sup>3</sup>. A pair of  $10^9$  particle realizations of flat cold, dark matter (CDM) cosmologies are evolved with particle mass equivalent to that associated with the extended halos of bright galaxies. The simulations are designed to discover the rarest and most massive clusters (by maximizing volume) while retaining force and mass resolution sufficient to determine global quantities (mass, shape, low-order kinematics) for objects more massive than poor groups of galaxies ( $\sim 5 \times 10^{13} h^{-1} M_\odot$ ). To facilitate comparison to observations, we generate output that traces the dark matter structure along the past light-cone of two observing locations within the computational volume. These virtual *sky surveys*, along with usual fixed proper time *snapshots*, provide samples of millions of clusters that enable detailed statistical studies. We publish the cluster catalogs here as electronic tables.

In this paper, we extend the detailed cluster mass function analysis of J01 to the sky survey output, updating results using a cluster finding algorithm with improved completeness properties for poorly resolved groups. X-ray temperatures are estimated by assuming a constant proportionality factor  $\beta$  between the specific energies of dark matter and the ICM. Using subvolumes of the  $z=0$  outputs, we calibrate the uncertainty in  $\sigma_8$  arising from sample, or *cosmic*, variance in the local temperature function. We find this error to be comparable to the stated overall errors of previous studies. We then study the implications that this normalization uncertainty, along with other degrees of freedom associated with connecting light to mass, have on tests of cosmology using high redshift cluster observations.

In §2, we describe the simulations, including the process of generating sky survey output, and the model used to convert dark matter properties to X-ray observables. The cluster mass function is examined in §3. Million cluster samples at  $z=0$  are used to determine the best fit parameters of the Jenkins mass function, and we show that this function reproduces well the sky survey populations extending to  $z > 1$ . The interplay between the fit parameters,  $\sigma_8$  and the normalization of cluster masses is explored, and this motivates a procedure for transforming the discrete cluster sets to mimic variation in  $\sigma_8$ .

In §4, we use the observational data set analyzed by Pierpaoli *et al.* to calibrate the specific energy factor  $\beta$  for each model. We then investigate the effects of cosmic variance on  $\sigma_8$ . In §5, we explore properties of the high

redshift cluster population, emphasizing uncertainties resulting from  $\sigma_8$  error, intracluster gas evolution and possible X-ray selection biases under low signal-to-noise conditions. The effective  $\sigma_8$  transformations developed in §3 are used to explore cluster yields anticipated from upcoming SZ surveys, and the median redshift in mass-limited samples is identified as a robust cosmological discriminant. Characteristic properties of the  $\Lambda$ CDM cluster population are summarized in §6, and we review our conclusions in §7.

## 2. HUBBLE VOLUME SIMULATIONS

After an upgrade in 1997 of the Cray T3E at the Rechenzentrum Garching<sup>1</sup> to 512 processors and 64Gb of memory, we carried out a pair of one billion ( $10^9$ ) particle simulations over the period Oct 1997 to Feb 1999. A memory-efficient version of Couchman, Pearce and Thomas' Hydra N-body code (Pearce & Couchman 1997) parallelized using *shmem* message-passing utilities was used to perform the computations. MacFarland *et al.* (1998) provide a description and tests of the parallel code.

We explore two cosmologies with a flat spatial metric, a  $\Lambda$ CDM model dominated by vacuum energy density (a non-zero cosmological constant) and a  $\tau$ CDM model dominated by non-relativistic, cold dark matter. The  $\tau$ CDM model completed May 1998 while the  $\Lambda$ CDM model finished Feb 1999. Published work from these simulations includes an extensive analysis of counts-in-cells statistics (to  $> 10^{\text{th}}$  order) by Colombe *et al.* (2000) and Szapudi *et al.* (2000), investigation of the clustering behavior of clusters (Colberg *et al.* 2000; Padilla & Baugh 2001), analysis of two-point function estimators (Kerscher, Szapudi & Szalay 2000), a description of the mass function of dark matter halos (J01), a study of confusion on the X-ray sky due to galaxy clusters (Voit, Evrard & Bryan 2001), statistics of pencil-beam surveys (Yoshida *et al.* 2000). Kay, Liddle & Thomas (2001) use the sky survey catalogs to predict Sunyaev-Zel'dovich (SZ) signatures for the planned *Planck Surveyor* mission while Outram *et al.* (2001) use the deep mock  $\Lambda$ CDM surveys to test analysis procedures for the 2dF QSO Redshift Survey.

### 2.1. Simulation description

Table 1 summarizes parameter values for each model, including the final epoch matter density  $\Omega_m$ , vacuum energy density  $\Omega_\Lambda$ , power spectrum normalization  $\sigma_8$ , starting redshift  $z_{\text{init}}$ , simulation side length  $L$  and particle mass  $m$ .

Values of  $\sigma_8$  were chosen to agree approximately with both the amplitude of temperature anisotropies in the cosmic microwave background as measured by COBE and with the nearby space density of rich X-ray clusters. The degree of uncertainty in these constraints allows the final space density of clusters as a function of mass to differ between the two simulations. However, as we discuss below, it is possible to ensure that the observed space density of clusters as a function of X-ray temperature is matched in both models by adjusting a free factor  $\beta$  used to link X-ray temperature to dark matter velocity dispersion. We derive an approximate scaling  $\beta \sim \sigma_8^{5/3}$  in §4.4 below.

To initiate the numerical experiments, particle posi-

<sup>1</sup>The Max-Planck Society Computing Center at Garching.

TABLE 1  
MODEL PARAMETERS.

Model	$\Omega_m$	$\Omega_\Lambda$	$\sigma_8$	$z_{init}$	$L^a$	$m^b$
$\Lambda$ CDM	0.3	0.7	0.9	35	3000	2.25
$\tau$ CDM	1.0	0	0.6	29	2000	2.22

<sup>a</sup>Cube side length in  $h^{-1}$  Mpc.

<sup>b</sup>Particle mass in  $10^{12} h^{-1} M_\odot$ .

tions and momenta at  $z_{init}$  are generated by perturbing a replicated ‘glass’ of one million particles with a set of discrete waves randomly drawn from power spectra computed for each cosmology. Initial Fourier modes of the applied perturbations have amplitudes drawn from a Gaussian distribution with variance given by the power spectrum  $P(k) = T(k)P_{\text{prim}}(k)$ . A Harrison-Zel'dovich primordial spectrum  $P_{\text{prim}}(k) \propto k$  is assumed for both models. For the  $\Lambda$ CDM model, the transfer function  $T(k)$  is computed using CMBFAST (Seljak & Zaldarriaga 1996) assuming  $h = 0.7$  and baryon density  $\Omega_b h^2 = 0.0196$  (Burles & Tytler 1998). The  $\tau$ CDM model uses transfer function  $T(k) = (1 + [aq + (bq)^{3/2} + (cq)^2])^{-1/\nu}$ , where  $q = k/\Gamma$ ,  $\Gamma = \Omega_m h$ ,  $a = 6.4 h^{-1}$  Mpc,  $b = 3 h^{-1}$  Mpc,  $c = 1.7 h^{-1}$  Mpc and  $\nu = 1.13$  (Bond & Efstathiou 1984).

The simulations are designed to resolve the collapse of a Coma-sized cluster with 500 particles. Although this resolution is sufficient to capture only the later stages of the hierarchical build-up of clusters, convergence tests (Moore *et al.* 1998; Frenk *et al.* 1999) show that structural properties on scales larger than a few times the gravitational softening length are essentially converged. From tests presented in J01 and in an Appendix to this work, cluster identification is robust down to a level of about 20 particles. Using  $M_{\text{Coma}} = 1.1 \times 10^{15} h^{-1} M_\odot$  (White *et al.* 1993), leads to particle mass  $2.2 \times 10^{12} h^{-1} M_\odot$  in both models, comparable to the total mass within  $\sim 300 h^{-1}$  kpc of bright galaxies (Fischer *et al.* 2000; Smith *et al.* 2001; Wilson *et al.* 2001). The mass associated with one billion particles at the mean mass density sets the length  $L$  of the periodic cube used for the computations, resulting in a Hubble Length  $L = c/H_0 = 3 h^{-1}$  Gpc for the  $\Lambda$ CDM model and  $L = 2 h^{-1}$  Gpc for  $\tau$ CDM.

A Newtonian description of gravity is assumed, appropriate for weak-field structures. In the linear regime, this treatment generates growth of density perturbations that matches the expected behavior from a full general relativistic treatment. A non-retarded gravitational potential is employed because the peculiar acceleration converges on scales well below the Hubble length. The good agreement between the higher-order clustering statistics of the simulations and expectations derived from an extended perturbation theory treatment of mildly-nonlinear density fluctuations provides indirect evidence that this treatment of gravity is accurate (Colombi *et al.* 2000; Szapudi *et al.* 2000).

Gravitational forces on each particle are calculated as

a sum of a long-range component, determined on a uniform spatial grid of  $1024^3$  elements using Fast Fourier Transforms, and a short-range component found by direct summation. The latter force is softened with a spline-smoothing roughly equivalent to a Plummer law gravitational potential  $\phi(r) \propto (r^2 + \varepsilon^2)^{-1/2}$  with smoothing scale  $\varepsilon = 0.1 h^{-1}$  Mpc. A leapfrog time integration scheme is employed with 500 equal time steps for each calculation.

Processor time for these computations was minimized by employing a parallel algorithm well matched to the machine architecture (MacFarland *et al.* 1998) and by simulating large volumes that entail a minimum of message passing overhead. The Cray-T3E offers high interprocessor communication bandwidth along with a native message-passing library (*shmem*) to control data flow. A two-dimensional, block-cyclic domain decomposition scheme allocates particles to processors. Each processor advances particles lying within a disjoint set of rectangular regions of dimension  $L \times (L/32) \times (L/16)$  that subdivide the computational space. Each calculation required approximately 35,000 processor hours, or three days of the 512-processor machine. This corresponds to advancing roughly 4000 particles per second on an average step. The computations were essentially limited by I/O bandwidth rather than cpu speed. Execution was performed in roughly twenty stages spanning a calendar time of three to four months, with data archived to a mass storage system between stages. Approximately 500 Gb of raw data were generated by the pair of simulations.

## 2.2. Sky survey output

In addition to the traditional simulation output of snapshots of the particle kinematic state at fixed proper time, we introduce here sky survey output that mimics the action of collecting data along the past light-cone of hypothetical observers located within the simulation volume. The method extends to wide-angle surveys an approach pioneered by Park & Gott (1991) in simulating deep, pencil-beam observations. Since there is no preferred location in the volume, we chose two survey origins, located at the vertex and center of the periodic cube for convenience.

In a homogeneous world model, a fixed observer at the present epoch  $t_0$  receives photons emitted at  $t < t_0$  that have traversed comoving distances  $r(t) = c \int_t^{t_0} dt a^{-1}(t)$  where  $a(t)$  is the scale factor of the metric ( $a(t_0) = 1$ ) and  $c$  the speed of light. The set of events lying along the continuum of concentric spheres  $\{t, \vec{r}(t)\}$  for  $t < t_0$  defines the

TABLE 2  
LIGHT-CONE SKY SURVEYS.

Name	center	solid angle	$z_{\max} (\Lambda)$	$z_{\max} (\tau)$
MS	$(L/2, L/2, L/2)$	$4\pi$	0.57	0.42
VS	$(0, 0, 0)$	$4\pi$	0.57	0.42
PO	$(0, 0, 0)^a$	$\pi/2$	1.46	1.25
NO <sup>b</sup>	$(L, L, L)^a$	$\pi/2$	1.46	1.25
DW	$(0, 0, 0)^a$	$10^\circ \times 10^\circ$	4.4	4.6
XW	$(0, 0, 0)$	$16^\circ \times 76^\circ$	6.8	—

<sup>a</sup>Orientation centered on cube diagonal.

<sup>b</sup>NO/PO have opposite orientations about a common center.

past light-cone for that observer. In the discrete environment of the numerical simulation, we construct the light-cone survey by choosing spherical shells of finite thickness such that each particle's state is saved at a pair of consecutive timesteps that bound the exact time of intersection of the light-cone with that particle's trajectory. Defining  $t_i$  as the proper time at step  $i$  of the computation, we choose inner and outer radii  $(1 - \eta)r(t_{i+1})$  and  $(1 + \eta)r(t_{i-1})$ . Here  $\eta \simeq 0.02$  is a small parameter that safeguards against a particle appearing only once in the output record due to peculiar motion across the discrete shells during a step. The inner radius is set to zero on the final two steps of the calculation.

With successive states for particles in the output record, a linear interpolation is performed to recover the original second-order time accuracy of the leap-frog integrator. Given a particle's position relative to the survey origin  $\vec{x}_i$  and, at the subsequent step,  $\vec{x}_{i+1} \equiv \vec{x}_i + \Delta\vec{x}$ , we solve for interpolation parameter  $\alpha$  defining position  $\vec{x} = \vec{x}_i + \alpha\Delta\vec{x}_i$  such that  $|\vec{x}| = r(t_i + \alpha\Delta t)$ , with  $\Delta t$  the timestep. For a spherical survey, this implies

$$\alpha = \frac{r^2(t_i) - x_i^2}{2(\vec{x}_i \cdot \Delta\vec{x} + r(t_i)\Delta r)} \quad (4)$$

with  $\Delta r = r(t_i) - r(t_{i+1}) > 0$ . After solving for  $\alpha$ , the particle's position and velocity are interpolated and the result stored to create the processed light-cone data sets. Comoving coordinates and physical velocities are stored as two-byte integers, sufficient to provide  $\sim \varepsilon/10$  positional accuracy and km/s accuracy in velocity. Data are stored in binary form in multiple files, each file covering a subcube of side  $L/16$  of the entire computational volume. Tape copies of the particle data sets can be ordered at the Virgo archive site <http://www.mpa-garching.mpg.de/Virgo>.

The scale  $L$  and comoving distance-redshift relation for each model, shown in Figure 1, determine the redshift extents of the surveys listed in Table 2. Two principal survey types — spheres and octants — extend to distances  $L/2$  and  $L$ , respectively. From the cube center, the MS full-sphere surveys extend to redshifts  $z_{\max} = 0.57$  ( $\Lambda$ CDM) and 0.42 ( $\tau$ CDM). From the origin and its diagonally opposing image, octant surveys (PO and NO, respectively) map to redshifts 1.46 ( $\Lambda$ CDM) and 1.25 ( $\tau$ CDM). The sur-

veys have opposite orientation, with both viewing the interior region of the computational space. The VS sphere centered on the origin is created using translational symmetries of separate octant surveys conducted from the eight vertices of the fundamental cube. The interior portion of the PO and NO surveys are thus subsets (opposite caps) of the VS survey. The extent of the spheres and octants leads to a sampling of the entire simulation volume roughly once for each survey type. In terms of cosmic time, the octants extend over the last 74% and 71% of the age of the universe ( $\Lambda$ CDM and  $\tau$ CDM, respectively), equivalent to roughly a 10 Gyr look-back time.

In addition to these surveys, smaller solid angle wedge surveys reach to greater depth. A  $10 \times 10$  sq deg deep wedge (DW) extends along the cube diagonal to the opposite corner and reaches redshifts 4.4 ( $\Lambda$ CDM) and 4.6 ( $\tau$ CDM). For the  $\Lambda$ CDM model only, a  $16 \times 76$  sq deg extended wedge (XW) uses periodic images of the fundamental cube to reach  $z_{\max} = 6.8$ . This wedge is an extension of the PO survey.

### 2.3. Connecting to X-ray observations

Connecting to observations of clusters requires a model that relates luminous properties to the underlying dark matter. We focus here on the ICM temperature  $T$  under the assumption that both  $T$  and the dark matter velocity dispersion  $\sigma_v$  are related to the underlying dark matter gravitational potential through the virial theorem (Cavaliere & Fusco-Femiano 1976). Empirical support for this assumption comes from the observation that  $T \sim \sigma_{\text{gal}}^2$  (e.g., Wu, Xue & Fang 1999), the scaling expected if both galaxies and the ICM are thermally supported within a common potential. High resolution simulations of galaxy formation within a cluster indicate that  $\sigma_{\text{gal}}$  should accurately reflect the dark matter  $\sigma_v$  except for the brightest, early-type galaxies which display a mild  $\sim 25\%$  bias toward lower velocity dispersion (Springel *et al.* 2000).

Rather than map  $T$  to  $M$  directly, we prefer to use a one-to-one mapping between  $T$  and dark matter velocity dispersion  $\sigma_v$ . This approach has the advantage of naturally building in scatter between  $T$  and  $M$  at a fractional amplitude  $\sim 10\%$  that is consistent with expectations from direct, gas dynamic modeling (e.g., Mathiesen

& Evrard 2001; Thomas *et al.* 2001). We therefore assume that dark matter velocity dispersion maps directly to X-ray temperature and introduce the ratio of specific energies  $\beta \equiv \sigma_v^2 / (kT/\mu m_p)$ , where  $k$  is Boltzmann's constant,  $\mu$  the mean molecular weight of the plasma and  $m_p$  the proton mass, as an adjustable parameter. We fit  $\beta$  by requiring that the models match the local temperature function.

Varying the power spectrum normalization  $\sigma_8$  produces calculable shifts in the space density of clusters as a function of mass and velocity dispersion. Values of  $\beta$  required to fit X-ray observations are thus dependent on  $\sigma_8$ , and we derive this dependence in §4.4 below.

### 3. CLUSTER POPULATIONS

We begin by visualizing the evolution of clustering in the octant surveys. Thin slices of the matter density extending to  $z=1.25$  are presented in comoving and redshift space. The illustrations, offer a glimpse into the future of very deep, wide-angle galaxy surveys.

Details of the cluster finding algorithm are presented, and fits to the  $z=0$  mass functions performed for  $\Delta=200$ . A simple model for evolving the fit parameters with redshift in the  $\Lambda$ CDM case is presented, and predictions based on these fits are then compared to the discrete cluster populations of the sky surveys in three broad redshift intervals.

We provide additional details in two appendices. Appendix A compares output of the SO algorithm employed here to that used by J01. Appendix B presents a model for extending the mass function fits under variation of the mass scale. The model allows fit parameters to be estimated for thresholds values  $\Delta \neq 200$ . More generally, it provides a means to effectively transform the discrete cluster sample under variation of  $\sigma_8$ . This functionality is used in §5 to investigate the sensitivity of Sunyaev–Zel'dovich cluster search yields to  $\sigma_8$  uncertainty.

#### 3.1. Evolution of the matter distribution

In Figure 2, we present maps of the Lagrangian smoothed mass density in slices through the octant surveys that extend to  $z=1.25$ . Horizontal and vertical maps show comoving and redshift space representations, respectively. Since the Hubble Length far exceeds the characteristic clustering length of the mass, the feature most immediately apparent in the density maps is their overall homogeneity. Gravitational enhancement of the clustering amplitude over time is evident from the fact that the density fluctuations are more pronounced near the survey origin (vertex of each triangular slice) compared to the edge. The effect is subtle in this image because the dynamic range in density, from black to white, spans three orders of magnitude, much larger than the linear growth factors of 1.8 ( $\Lambda$ CDM) and 2.2 ( $\tau$ CDM) for large-scale perturbations in the interval shown.

To verify the accuracy of the clustering evolution in the octant surveys, we show in Figure 3 the behavior of the rms amplitude of density fluctuations  $\langle \delta^2 \rangle^{1/2}$ , where  $\delta \equiv \rho/\bar{\rho}_m(z) - 1$ , within spheres encompassing, on average, a mass of  $2.2 \times 10^{15} h^{-1} M_\odot$  (1000 particles). Points in the figure show  $\langle \delta^2 \rangle^{1/2}$  determined by randomly sampling locations within twenty radial shells of equal volume in the octant surveys. Values are plotted at the volume-weighted redshift of each shell. Solid lines are not fits,

but show the expectations for  $\langle \delta^2 \rangle^{1/2}$  based on linear evolution of the input power spectrum. Deviations between the measured values and linear theory, shown in the upper panels of Figure 3, are at the 1% level. Although we do not attempt here to model these deviations explicitly, the higher-order clustering properties of these simulations at the final epoch are well described by expectations from an extended perturbation theory treatment of fluctuation evolution (Szapudi *et al.* 2000).

The orientation of the slice shown in Figure 2 is chosen to include the most massive cluster in the both  $\Lambda$ CDM octant surveys. It lies at the surprisingly high redshift  $z=1.04$ . The inset in Figure 2, a blow-up of the region surrounding this cluster, shows that it is actively forming from mergers fed by intersecting filaments. In Figure 4, we show a close-up of the redshift space structure in  $75,000 \text{ km s}^{-1}$  wide regions centered at  $z=1.1$  and lying just interior to the vertical edges of the redshift-space views of Figure 2. The grey-scale shows only overdense material  $\delta > 0$ . The most massive cluster, with rest-frame line-of-sight velocity dispersion  $1964 \text{ km s}^{-1}$ , produces the  $\sim 16,000 \text{ km s}^{-1}$  sized ‘finger-of-God’ feature in the lower right.

Along with this extreme object, close inspection of Figure 4 reveals many more smaller fingers representing less massive clusters in the  $\Lambda$ CDM image. In comparison, the number of similar clusters in the  $\tau$ CDM model is much smaller. It is this difference that motivates high redshift cluster counts as a sensitive measure of the matter density parameter  $\Omega_m$ . To perform quantitative analysis of the cluster population, we turn now to detailing the method used to identify clusters in the particle data sets.

#### 3.2. Cluster finding algorithm

A number of methods have been developed for identifying clusters within the particle data sets of cosmological simulations. We refer the reader to J01, White (2000) and Lacey & Cole (1994) for discussion and intercomparisons of common approaches. Two algorithms are employed by J01. One is a percolation method known as ‘friends-of-friends’ (FOF) that identifies a group of particles whose members have at least one other group member lying closer than some threshold separation. The threshold separation, typically expressed as a fraction  $\eta$  of the mean interparticle spacing, is a parameter whose variation leads to families of groups, referred to as FOF( $\eta$ ), with favorable nesting properties (Davis *et al.* 1985).

The other algorithm of J01 is a spherical overdensity (SO) method that identifies particles within spherical regions, centered on local density maxima, whose radius is set by a mean enclosed iso-density condition. We use here an SO algorithm that differs slightly from that of J01. The iso-density condition requires the mean mass density within radius  $r_\Delta$  to be a factor  $\Delta$  times the critical density  $\rho_c(z)$  at redshift  $z$ . J01 define spherical regions that are overdense with respect to the mean background, rather than the critical mass density. For clarity, we refer to the approaches as ‘mean SO’ and ‘critical SO’ algorithms, respectively. If not stated explicitly, reference to SO( $\Delta$ ) should be read as the critical case evaluated at contrast  $\Delta$ . By definition, a critical SO( $\Delta$ ) population is identical to a mean SO( $\Delta/\Omega_m$ ).

TABLE 3  
FIT PARAMETERS FOR  $\ln \sigma^{-1}(M)$ .<sup>a</sup>

Model	$\sigma_{15}$	$a$	$b$
$\Lambda$ CDM	0.578	0.281	0.0123
$\tau$ CDM	0.527	0.267	0.0122

<sup>a</sup>equation (7).

Details of our method, which employs a code independent of that used by J01, are given in an Appendix. Also included there is a discussion of completeness properties for low particle number groups based on direct comparison of group catalogs from the two independent algorithms.

### 3.3. Mass function fits at $z=0$

Based on coadding 22 snapshots of 11 Virgo Consortium simulations ranging in scale from  $84.5 h^{-1}$  Mpc to  $3000 h^{-1}$  Mpc, J01 showed that the space density of clusters defined by either FOF(0.2) or SO(180) algorithms are well described by a single functional form when expressed in terms of  $\ln \sigma^{-1}(M)$ , where  $\sigma^2(M)$  is the variance of the density field smoothed with a spherical top-hat filter that encloses mass  $M$  at the mean density. Defining the mass fraction  $f(\sigma^{-1})$  by

$$f(\sigma^{-1}) \equiv \frac{M}{\bar{\rho}_m(z)} \frac{dn_{cum}(M)}{d \ln \sigma^{-1}} \quad (5)$$

with  $\bar{\rho}_m(z)$  the background matter density at the epoch of interest and  $n_{cum}(M)$  the cumulative number density of clusters of mass  $M$  or smaller, the general form found by J01 for the mass function is

$$f(\sigma^{-1}) = A \exp[-|\ln \sigma^{-1} + B|^\epsilon] \quad (6)$$

where  $A$ ,  $B$  and  $\epsilon$  are fit parameters. Values of these parameters depend on the particular cluster finding scheme implemented, but J01 show them to be independent of cosmology and redshift when cluster masses are based on algorithms tied to the mean mass density. The amplitude  $A$  sets the overall mass fraction in collapsed objects,  $e^B$  plays the role of a (linearly evolved) collapse perturbation threshold, similar to the parameter  $\delta_c$  in the Press-Schechter model or its variants, and  $\epsilon$  is a stretch parameter that provides the correct shape of the mass function at the very dilute limit. For the FOF(0.2) group catalogs, J01 find that  $A=0.315$ ,  $B=0.61$  and  $\epsilon=3.8$  provide a fit that describes all of the numerical data to  $\lesssim 20\%$  precision over eight orders of magnitude in number density.

We fit here the SO mass function by employing a quadratic relation describing the filtered power spectrum shape

$$\ln \sigma^{-1}(M) = -\ln \sigma_{15} + a \ln M + b (\ln M)^2 \quad (7)$$

where  $M$  is mass in units of  $10^{15} h^{-1} M_\odot$  and the *rms* fluctuation amplitude  $\sigma_{15}$  at that mass scale is simply related to the fiducial power spectrum normalization by

$\ln \sigma_{15} = \ln(\sigma_8) + \text{const.}$  Table 3 lists parameters of the fit to equation (7). The maximum error in the fit is 2% in  $\ln \sigma^{-1}$  for masses above  $10^{13} h^{-1} M_\odot$ . For both models, the effective logarithmic slope,

$$\alpha_{\text{eff}}(M) \equiv d \ln \sigma^{-1}(M) / d \ln M = a + 2b \ln M, \quad (8)$$

slowly varies between  $0.2 - 0.3$  from  $10^{13}$  to  $10^{15.5} h^{-1} M_\odot$ . The Jenkins mass function (JMF) expression for the differential number density  $n_{\text{JMF}}(M, z) d \ln M$  as a function of mass and redshift

$$n_{\text{JMF}}(M, z) = \frac{A \bar{\rho}_m(z)}{M} \alpha_{\text{eff}}(M) \exp[-|\ln \sigma^{-1}(M) + B|^\epsilon] \quad (9)$$

is the form we fit to the simulated cluster catalogs.

The critical SO(200) mass functions at  $z=0$  for both models are shown in Figure 5, derived from samples of 1.39 million ( $\Lambda$ CDM) and 1.48 million ( $\tau$ CDM) clusters above  $5 \times 10^{13} h^{-1} M_\odot$ . Fits to equation (9) are shown as dotted lines, with fit parameters listed in Table 4. The upper panels of Figure 5 show the fractional deviations  $\delta n/n = n/n_{\text{JMF}} - 1$  in bins of width 0.12 in  $\ln M$ . Error bars assume Poisson statistics. For bins with 100 or more clusters ( $M_{200} \lesssim 2 \times 10^{15} h^{-1} M_\odot$ ), the *rms* deviations  $\langle (\delta n/n)^2 \rangle^{1/2}$  are  $\lesssim 3\%$  (Table 4). At larger masses, the fit slightly overestimates the measured density.

The high statistical precision of these fits is a lower bound on the absolute accuracy of the mass function calibration. Based on the fits performed by J01 to a large ensemble of simulations covering a wider dynamic range in scale than the HV models alone, we estimate that the normalization  $A$  may be systematically low by  $\sim 10\%$  (see Appendix). Considering that this degree of uncertainty in  $A$  corresponds to an uncertainty in mass of only 2–3%, this accuracy is sufficient for the practical purpose of comparing to current and near future observations where the level of systematic uncertainty in mass is at least 10%.

Another estimate of systematic error in space density is provided by comparing our results to the recent large simulations of Bode *et al.* (2001). Their  $1 h^{-1}$  Gpc  $\Lambda$ CDM simulation assumes identical cosmological parameters to our  $\Lambda$ CDM model, but uses a particle mass and gravitational softening factors of 30 and 7 times smaller, respectively. Bode *et al.* employ a measure of mass within a comoving radius  $1.5 h^{-1}$  Mpc; this scale encompasses a critical density contrast of 200 at the present epoch for mass  $M_{200} = 7.94 \times 10^{14} h^{-1} M_\odot$ . From their Figure 6, the space density of clusters above that mass scale is

TABLE 4  
SO(200) MASS FUNCTION PARAMETERS.<sup>a</sup>

Model	$A$	$B$	$\epsilon$	$\langle(\delta n/n)^2\rangle^{1/2}$
$\Lambda$ CDM	0.22	0.73	3.86	0.026
$\tau$ CDM	0.27	0.65	3.77	0.028

<sup>a</sup>equation (9).

$10^{-6.6} \sim 2.5 \times 10^{-7} h^3 \text{ Mpc}^{-3}$ . In our  $27h^{-3} \text{ Gpc}^3$  volume, we find 6499 clusters above this mass limit, implying a space density  $2.4 \times 10^{-7} h^3 \text{ Mpc}^{-3}$ . A similar level of agreement is found by J01 in comparing the HV results for  $f(\ln \sigma^{-1})$  to those of Governato *et al.* (1999).

Figure 5 shows that the two models do not produce identical mass functions at the present epoch; the  $\Lambda$ CDM space density is lower by a factor  $\sim 4$  than that of  $\tau$ CDM. Two factors combine to make this difference. The first is that our chosen values of  $\sigma_8$  straddle the constraint derived from fitting the local X-ray cluster space density, such as that quoted in equation (3). The sense of the difference — the  $\Lambda$ CDM model has lower amplitude, and the  $\tau$ CDM higher, by about 10% — works in the direction of producing fewer massive clusters in the  $\Lambda$ CDM model. The second factor leading to smaller  $\Lambda$ CDM masses is our choice of fixed critical threshold  $\Delta = 200$ . Previous work has typically employed the lower  $\Omega_m(z)$ -dependent thresholds derived by Eke *et al.* (1996) from the spherical collapse solutions of Lahav *et al.* (1991) and Lilje (1992). For  $\Omega_m = 0.3$ , Eke *et al.* calculate critical threshold  $\Delta = 97.2$ , and J01 use this threshold, expressed as mean SO(324), to define clusters in the  $\Lambda$ CDM model at  $z = 0$ .

### 3.4. Sky survey cluster populations

We define cluster catalogs in the sky survey output using the same SO algorithm applied to the snapshots at fixed proper time. A minor modification for the  $\Lambda$ CDM model must be made in order to define the threshold  $\Delta$  with respect to the critical, rather than the mean, mass density. Given the metric distance from a cluster's center to the survey origin, calculation of the critical density is done via the redshift-distance relation and the definition  $\rho_c(z) = \rho_c(0)[\Omega_m(1+z)^3 + \Omega_\Lambda]$  for flat cosmologies.

For the choice  $\Delta = 200$ , Table 5 lists counts of clusters identified in the sky survey catalogs above mass limits  $5 \times 10^{13} h^{-1} \text{ M}_\odot$ ,  $10^{14} h^{-1} \text{ M}_\odot$  and  $10^{15} h^{-1} \text{ M}_\odot$ . The lower mass limit corresponds to 22 particles and the maximum redshifts of the catalogs are given in Table 2. Total counts of 1.5 and 0.9 million clusters provide large statistical samples to use, for example, as a basis for Monte Carlo studies of observational survey expectations.

At the massive end of the spectrum, small numbers of objects put the finite size of the visible universe into context and provide additional motivation for near-future surveys to define a complete sample of the most massive clusters in the universe. Only a few hundred Coma-like or larger clusters are expected on the sky at all redshifts in either cosmology.

Figure 6 shows redshift-space maps of clusters with  $M_{200} > 10^{14} h^{-1} \text{ M}_\odot$  and  $z \leq 1.25$  in  $3 \times 90$  deg strips taken from the PO octant surveys of the  $\tau$ CDM (left) and  $\Lambda$ CDM (right) models. The surveys display markedly different evolution at  $z > 0.5$ . As known from previous N-body modeling (Efstathiou, Frenk & White 1993; Eke, Cole & Frenk 1996; Bahcall Fan & Cen 1997), distant clusters are more abundant in low density cosmologies. Within the 3 deg slice — a width roughly equivalent to two Sloan Digital Sky Survey scans — the  $\Lambda$ CDM model contains 3084 clusters above the  $10^{14} h^{-1} \text{ M}_\odot$  mass limit, half lying beyond  $z = 0.70$ . The  $\tau$ CDM model contains 1122 clusters, with median  $z = 0.39$ .

The sky surface density of clusters within three broad redshift intervals are shown as a cumulative function of mass in Figure 7. The ranges in redshift are chosen to represent three classes of observation: local,  $z < 0.2$ ; intermediate,  $0.2 \leq z < 0.5$ , and high,  $0.5 \leq z < 1.2$ . Within each panel, counts measured within the octant surveys are shown by the data points while solid lines show the number expected from integrating the Jenkins mass function, equation (9), over the appropriate volume  $N(> M) = \int_{z_{\min}}^{z_{\max}} dz (dV/dz) \int_{\ln M}^{\infty} d \ln M' n_{\text{JMF}}(M', z)$ . An upper limit of  $10^{16} h^{-1} \text{ M}_\odot$  for the mass integral is used in practice.

For  $\tau$ CDM, the integral is performed using the fit parameters determined at  $z = 0$  (Table 4). For  $\Lambda$ CDM, we must recognize the fact that, because  $\Omega_m(z)$  varies along the light-cone, the fit parameters will evolve with redshift. As  $\Omega_m(z)$  approaches one at high redshifts, we expect the parameters to converge to the  $\tau$ CDM values. Since differences in  $A$ ,  $B$  and  $\epsilon$  between the two models are small at  $z = 0$ , we take a simple approach and vary the parameters linearly in  $\Omega_m$ . For example, we assume for  $A$  that

$$A(\Omega_m) = (1 - x)A(1) + xA(0.3), \quad (10)$$

where  $x \equiv (1 - \Omega_m)/0.7$  and  $A(1)$  and  $A(0.3)$  are the  $z = 0$  fit parameters for  $\tau$ CDM and  $\Lambda$ CDM from Table 4. Similar interpolations are assumed for  $B$  and  $\epsilon$ .

The predictions of this model agree very well with the measured counts in the octant surveys. The model is accurate to  $\lesssim 10\%$  in number for  $\Lambda$ CDM at all masses and redshifts shown. Similar accuracy is displayed for the  $\tau$ CDM model at low and intermediate redshifts, but the model systematically underestimates counts in the high redshift interval by  $\sim 25\%$ .

Dashed lines in Figure 7 show numbers expected by the Press-Schechter model in its simplest form (see J01 for de-

TABLE 5  
COUNTS OF CLUSTERS WITH  $hM_{200}/M_{\odot}$  ABOVE MASS LIMITS.

Survey	$\Lambda$ CDM			$\tau$ CDM		
	$5 \times 10^{13}$	$10^{14}$	$10^{15}$	$5 \times 10^{13}$	$10^{14}$	$10^{15}$
MS	564,875	178,223	322	377,043	102,742	120
VS	565,886	178,483	285	378,548	103,157	111
PO	255,083	64,608	45	107,900	22,853	10
NO	259,279	64,930	42	108,807	23,216	13
DW	5,238	1,316	1	1,833	411	0
Total	1,504,620	441,833	623	878,356	226,602	231

tails). For the  $\tau$ CDM model, the PS curve tends to underestimate the space density at high masses. For the  $\Lambda$ CDM model, the use of mass measured within a critical, rather than mean, mass density threshold leads to an offset in mass between the measured counts and PS curves at low redshifts. The offset declines at higher redshift as  $\Omega_m(z)$  approaches unity and, by coincidence, the mass offset in the high redshift interval  $0.5 \geq z < 1.2$  works in a manner that provides a good match to the simulated counts.

In the  $\Lambda$ CDM panels, we plot the  $\tau$ CDM JMF curves as dotted lines for comparison. At low redshifts, the two models exhibit an offset in the direction of  $\tau$ CDM being overabundant relative to  $\Lambda$ CDM, a difference already discussed in §3.3 for the  $z=0$  population. In the intermediate redshift interval, this offset is reversed at nearly all masses above the  $5 \times 10^{13} h^{-1} M_{\odot}$  limit. At high redshifts, the  $\Lambda$ CDM counts are typically an order of magnitude higher than those of  $\tau$ CDM.

This trend in redshift is examined more closely in Figure 8, where we plot the cumulative sky surface density of clusters above mass limits  $5 \times 10^{13}$ ,  $3 \times 10^{14}$ , and  $10^{15} h^{-1} M_{\odot}$  as a function of redshift. Points show the sky densities of clusters lying at redshift  $z$  or higher with masses above the stated limits (top to bottom, respectively), determined by combining the octant surveys of each model. Lines in the figure show the JMF expectations from integrating equation (9) using the linear evolution of the fit parameters, equation (10).

Comparison of the octant counts with the JMF expectations provides a measure of the incompleteness of the HV sky catalogs that arises from their finite redshift extent. At Coma mass scales ( $> 10^{15} h^{-1} M_{\odot}$ ), the catalogs are essentially complete, as fewer than one such object is expected over  $\pi$  steradian beyond the survey redshift limit. At  $3 \times 10^{14} h^{-1} M_{\odot}$ , the  $\Lambda$ CDM model octants are missing  $\sim 100$  clusters expected above  $z = 1.5$ , implying  $\sim 98\%$  completeness. The  $\tau$ CDM model at this mass limit is essentially complete; the small discrepancy between the measured and JMF counts at redshifts  $z \gtrsim 0.5$  reflects the systematic trend exhibited in Figure 7. At the mass scale of groups,  $5 \times 10^{13} h^{-1} M_{\odot}$ , the incompleteness becomes more significant. In the  $\Lambda$ CDM model, for example,  $\sim 15\%$  of the group population should lie at  $z > 1.5$ .

The  $\Lambda$ CDM model possesses a healthy population of very high redshift clusters. Across the whole sky, a cluster as massive as Coma is expected at redshifts as high

as 1.3. At  $z > 2.5$ , one  $3 \times 10^{14} h^{-1} M_{\odot}$  cluster should lie somewhere on the sky, joined by  $\sim 20,000$  others above  $5 \times 10^{13} h^{-1} M_{\odot}$ , nearly one per square degree. Before getting carried away by such seemingly firm predictions, we must investigate the effect of varying a degree of freedom that has so-far been kept fixed in the models: the amplitude of the fluctuation power spectrum  $\sigma_8$ .

#### 4. COSMIC VARIANCE UNCERTAINTY IN THE POWER SPECTRUM NORMALIZATION

The power spectrum amplitude  $\sigma_8$  sets the characteristic mass scale through equations (9) and (7). However, observational constraints on  $\sigma_8$  come not from direct measurements of mass, but from X-ray determinations of cluster temperatures. The relation between mass and temperature is a degree of freedom that must be taken into account in the modeling process.

In this section, we take advantage of this degree of freedom to tune  $\beta$ , the ratio of specific energies in dark matter and ICM gas, so that both models match the observed local temperature function. We then use the full  $z = 0$  volumes to calibrate the cosmic error in  $\sigma_8$  expected from sample variance in volumes of size comparable to those defined by present observations. The dependence of  $\beta$  on  $\sigma_8$  is derived in the dilute limit, and this analysis is used to revisit, in a more careful way, predictions for the high redshift cluster population in §5.

##### 4.1. Fitting local temperature observations

Pierpaoli, Scott & White (2001, hereafter PSW) provide the most recent study of the local temperature function and its constraints on  $\sigma_8$ . The sample of 38 clusters used in their analysis is adapted from the X-ray flux-limited sample of Markevitch (1998) and is designed as an essentially volume-limited sample within redshifts  $0.03 < z < 0.09$  and galactic latitude  $|b| > 20^{\circ}$  for clusters with  $kT \gtrsim 6$  keV. PSW update temperatures for 23 clusters in the Markevitch (1998) sample with values given in White (2000).

PSW note that the White temperature values, derived from ASCA observations using a multi-phase model of cluster cooling flow emission, tend to be hotter (by 14% on average), than those Markevitch obtained through a single-temperature fit after exclusion of a core emission. Based on recent high-resolution studies of cooling flows (David *et al.* 2001; McNamara 2001) that do not appear to

support the underlying cooling flow emission model used by White (2000), there is cause for concern that the increased temperatures may be artificial. We therefore revert to the original values of Markevitch (1998), and note that the resulting effect on the derived values of  $\beta$  is about 10%.

We use the data from Tables 3 and 4 of PSW and perform a maximum likelihood fit to determine values of  $\beta$  for each model. Our procedure is similar to that used by PSW<sup>2</sup>, but rather than use an analytic model as a reference, we use the binned  $z = 0$  differential velocity distribution  $n(\sigma_v)$  converted to a temperature function  $n(T; \beta)$  for  $\beta$  in the range 0.2 to 2. For a given  $\beta$ , 300 Monte Carlo realizations of the observational sample are generated, assuming Gaussian statistics and errors distributed equally in number (half positive, half negative) about the best fit value. To consider those clusters for which the selection volume is best defined and for which cluster ICM physics is better understood, a lower limit of 6 keV is applied to each random realization.

The analysis leads to most likely values  $\beta_{\Lambda} = 0.92 \pm 0.06$  and  $\beta_{\tau} = 1.20 \pm 0.06$  for the  $\Lambda$ CDM and  $\tau$ CDM models. The quoted 68% confidence uncertainties reflect only the temperature errors of the observations.

Figure 9 compares the cumulative number of clusters as a function of temperature in the observational sample to those of the simulations using the best-fit values of  $\beta$ . In each panel, the solid line uses the  $z = 0$  cluster population from the entire simulation volume while the dotted line shows clusters lying within  $0.03 < z < 0.09$  in the combined spherical (MS+VS) sky surveys. Differences between the snapshot and sky survey samples are due to sample variance in the very dilute limit and to evolution of the number density. Evolution is evidently small in the  $\Lambda$ CDM model but produces a  $\sim 10\%$  shift to cooler temperatures for  $\tau$ CDM. Because this shift is comparable to uncertainties from sample variance discussed next, we do not adjust the constraint on  $\beta_{\tau}$  derived from the full  $z = 0$  sample.

#### 4.2. Cosmic variance uncertainty in $\sigma_8$

Large-scale density fluctuations modify the development of smaller, non-linear structures (Kaiser 1984; Frenk *et al.* 1988). Slightly overdense regions are more advanced while underdense regions are retarded in their structure with respect to the global mean evolution. On the scale of the survey volume limit of the sample used by PSW and previous authors,  $5 \times 10^7 h^{-3}$  Mpc<sup>3</sup>, fluctuations in mass density of 1 – 2% about the mean are expected for the models simulated here. Clusters within a particular region of this size are a slightly biased representation of the cosmic average. This cosmic variance is a source of uncertainty in determinations of  $\sigma_8$  that has been ignored in previous studies.

An impression of the magnitude of this effect is given in Figure 10. Differential mass functions from 16 separate sky octants extending to  $z = 0.15$ , extracted from the MS and VS surveys, are shown for the  $\Lambda$ CDM model. Also shown are the best-fit  $\Lambda$ CDM  $z = 0$  mass function, along with mass functions obtained after varying  $\sigma_8$  in equation (9) by  $\pm 0.05$ . The 5 percent variation in  $\sigma_8$  roughly outlines the

range seen in the 16 octant samples.

We use the full volumes of the  $z = 0$  samples to calibrate this effect more precisely. We divide the full computational volumes into cubic cells of size  $375 h^{-1}$  Mpc ( $\Lambda$ CDM) and  $400 h^{-1}$  Mpc ( $\tau$ CDM). Offsetting the grid of cells by half a cell width along the principal axes and resampling generates totals of 4096 and 1000 samples of clusters in cubes of volume comparable to that sampled by the local temperature observations. Within each cube, we determine the maximum likelihood value of  $\sigma_8$  using the expected space density from equations (9), (7) and (10). We perform the analysis using mass as the independent variable, imposing a global mass cutoff for each model that leads, on average, to samples of 30 clusters within each cube.

The distributions of  $\sigma_8$  that result from this exercise, shown in Figure 11, are nearly log-normal with means 0.868 and 0.583 and standard deviations 0.064 and 0.050 in  $\ln(\sigma_8)$  ( $\Lambda$ CDM and  $\tau$ CDM, respectively). The small difference between the means and the input values of  $\sigma_8$  reflects the imperfect fit of the Jenkins mass function for the most massive clusters.

The scatter in maximum likelihood values derived from ( $\sim 400 h^{-1}$  Mpc)<sup>3</sup> volumes indicates that the local observed temperature sample will lead to a 90%-confidence error on  $\sigma_8$  of at least 10%.

#### 4.3. $M - T$ calibration and overall $\sigma_8$ uncertainty

As emphasized by previous studies, uncertainty in the calibration of  $p(M | T)$  is a significant source of error in  $\sigma_8$ . We can connect uncertainty in  $\sigma_8$  to uncertainty in absolute mass scale by solving for the zero in the total derivative of the mass function, equation (9). The result is

$$\frac{\Delta \sigma_8}{\sigma_8} = \alpha'(M) \frac{\Delta M}{M} \quad (11)$$

where, at large masses ( $\sigma(M) < e^B$ ),

$$\alpha'(M) = \left[ \alpha_{\text{eff}}(M) + \frac{1}{\epsilon (\ln \sigma^{-1}(M) + B)^{\epsilon-1}} \right]. \quad (12)$$

The sensitivity  $\alpha'(M)$ , plotted in Figure 12, asymptotes to a value 0.4 above  $\sim 5 \times 10^{14} h^{-1} M_{\odot}$  in both cosmologies. Below this mass,  $\alpha'(M)$  increases considerably, reaching unity at  $10^{14} h^{-1} M_{\odot}$ . The rarest, most massive clusters place the most sensitive limits on  $\sigma_8$ .

Attempts at calibrating the mass-temperature relation have been made using numerical simulations and observations. Simulation results by different groups compiled by Henry (2000) and PSW display an overall range of  $\sim 50\%$  in temperature at fixed mass, equivalent to a 75% range in mass if one assumes  $M \propto T^{3/2}$ . A complicating factor is that normalizations are typically quoted using a mass-weighted temperature, and this measure can differ systematically at the  $\sim 20\%$  level from the spectral temperatures derived from plasma emission modeling of the simulated ICM (Mathiesen & Evrard 2001). Observational attempts at calibrating the relation (Horner, Mushotzky & Scharf 1999; Nevalainen, Markevitch & Forman 2000; Finoguenov, Reiprich, & Böhringer 2001) display discrepancies of similar magnitude to the simulations. Part of this variance may reflect the fact that these analyses are

<sup>2</sup>We note a typographical error in their equation (18), which should read  $\ln \mathcal{L} = \sum_i [(\eta_i - 1)\mu_i + \eta_i \ln(1 - \exp(-\mu_i))]$ .

comparing  $T$  to estimators  $\mathcal{M}$  that vary in their degree of bias and noise with respect to the true mass  $M$ .

For the purpose of making definite calculations but with relatively little in the way of firm justification, we estimate the  $1\sigma$  uncertainty in the zero point of the mass-temperature relation to be  $\Delta M/M = 0.2$ . Assuming log-normal errors, this assumption allows the mass scale to range over a factor 1.8 at 90% confidence. We note that PSW assumed a temperature normalization error of 10%, and this translates into a 15% uncertainty in mass, somewhat smaller than the value used here.

From equation (11), the fractional error introduced in  $\sigma_8$  by the mass scale uncertainty is 8%. Combining this in quadrature with a 6% contribution from cosmic variance leads to an overall systematic uncertainty

$$|\Delta\sigma_8/\sigma_8|_{\text{sys}} = 0.10 \quad (1\sigma) \quad (13)$$

or a 16% uncertainty at 90% confidence.

The systematic uncertainty dominates the overall error budget. From the errors in  $\beta$  derived from the local temperature sample in §4.1 above, coupled with the relation between  $\beta$  and  $\sigma_8$  discussed in the following section, we estimate the statistical error in  $\sigma_8$  arising from the current local sample to be  $\sim 3 - 4\%$ . We employ a 10% standard deviation in  $\ln(\sigma_8)$  when exploring the statistics of high redshift clusters in §5.

#### 4.4. Degeneracy in $\beta$ and $\sigma_8$

The calibration uncertainty discussed above in terms of mass can be rephrased in terms of temperature or, equivalently for this study, the parameter  $\beta$  used to connect temperature to dark matter velocity dispersion. An advantage of  $\beta$  is that it can be determined independently from gas dynamic simulations that model the gravitationally coupled evolution of the ICM and dark matter. In a comparison study of twelve, largely independent simulation codes applied to the formation of a single cluster, Frenk *et al.* (1999) found good agreement among the computed values of  $\beta$  within  $\Delta=200$ , with mean and standard deviation  $\bar{\beta}=1.17 \pm 0.05$ .

At first glance, this determination agrees well with the  $\tau\text{CDM}$  value of  $\beta$  but is in mild ( $2.7\sigma$ ) disagreement with the  $\Lambda\text{CDM}$  value derived from the local temperature sample in §4.1. However, the uncertainties quoted previously for  $\beta$  are derived at the fixed values of  $\sigma_8$  used in the N-body simulations. To incorporate the additional sources of error in  $\sigma_8$  discussed above, we use the mass sensitivity, equation (11), and the virial scaling  $T \propto \beta^{-1} M^p$  with  $p \simeq 2/3$  exhibited by gas dynamic simulations of clusters to derive the scaling

$$\beta \propto \sigma_8^{p/\alpha'(M)} \sim \sigma_8^{5/3}. \quad (14)$$

An increase in  $\beta_\Lambda$  of 20%, sufficient to match the Frenk *et al.* simulation ensemble value, requires a 12% increase to  $\sigma_8=1.01$ . This value is within the range allowed by COBE microwave background anisotropy constraints for Hubble parameter  $h \sim 0.7$  (Eke, Cole & Frenk 1996). Incorporating the systematic error in  $\sigma_8$  leads to updated values  $\beta_\Lambda = 0.92 \pm 0.17$  and  $\beta_\tau = 1.20 \pm 0.17$ . Within the larger uncertainty, both values are in line with the gas dynamic simulation results of Frenk *et al.* (1999).

## 5. CLUSTERS AT HIGH REDSHIFT

We are now in a position to revisit the expected numbers of high redshift clusters, incorporating into the analysis the total uncertainty in power spectrum normalization. We begin by noting the advantage of predicting cluster counts as a function of X-ray temperature rather than mass, and compare the model predictions to the sky surface density of high redshift clusters from the EMSS catalog (Henry *et al.* 1992; Gioia & Luppino 1994). Using the redshift information available from the RDCS catalog (Rosati *et al.* 1998; Borgani *et al.* 1999b), we show how plausible models for ICM luminosity evolution can be constructed so that either cosmology provides an acceptable match to those data.

We then return to mass selected samples and explore the sensitivity of Sunyaev-Zel'dovich searches for distant clusters to  $\sigma_8$  uncertainty. Finally, the redshift evolution of characteristic mass and temperature scales at fixed sky surface density is used to compare  $\Lambda\text{CDM}$  and  $\tau\text{CDM}$  expectations against redshift and temperature extremes of the observed cluster population.

### 5.1. *X-ray cluster counts*

The fact that all models are constrained by observations of the local temperature function means that predictions of counts as a function of temperature incur smaller uncertainty than predictions of counts as a function of mass. The mass function requires separate knowledge of  $T_{15}$  and  $\sigma_8$  whereas the temperature function requires, effectively, only a unique combination of the pair. This advantage breaks down if the connection between ICM temperature and total mass (or velocity dispersion) evolves with redshift. Current observations support no evolution (Tran *et al.* 1999; Wu, Xue & Fang 1999), at least for the connection between galaxy velocity dispersion  $\sigma_{\text{gal}}$  and ICM  $T$ . We therefore assume a non-evolving  $\beta$  in order to examine the space density of clusters as a function of temperature at arbitrary redshift.

Figure 13 shows the range of cumulative counts expected as a function of temperature within the same three broad redshift intervals used in Figure 7. The range in counts shown within each panel corresponds to varying  $\ln \beta$  within its 90% confidence region for each model; specifically,  $0.70 \leq \beta_\Lambda \leq 1.20$  and  $0.97 \leq \beta_\tau \leq 1.48$ . The constraint to match local observations produces nearly completely overlap in the temperature functions of the two cosmologies at  $z < 0.2$ . At intermediate redshifts, the  $\Lambda\text{CDM}$  function steepens and shifts to hotter temperatures while the  $\tau\text{CDM}$  also steepens but shifts little at high temperatures.

In the high redshift interval, the 90% confidence regions for the counts in each model are just barely disjoint. Observations in this redshift range, based on the EMSS survey data and shown as the square in the upper panel of Figure 13, are consistent with the  $\Lambda\text{CDM}$  expectations and rule out  $\tau\text{CDM}$  at 95% confidence. The EMSS data point is based on three hot ( $kT > 8$  keV) and distant ( $z > 0.5$ ) clusters covering a search area of 278 sq deg (Henry 2000), leading to a sky surface density 0.011 per sq deg at  $z > 0.5$ . Larger statistical samples are certainly desired and a number are being assembled based on ROSAT observations; *e.g.*, RDCS (Rosati *et al.* 1998), Bright SHARC (Romer *et al.* 2000), MACS (Ebeling, Edge & Henry 2001).

Only a small degree of redshift evolution in  $\beta_\tau$  is needed to reduce the confidence in ruling out  $\tau$ CDM with the EMSS data. Additional information on the cluster population, such as the redshift distribution of X-ray flux-limited samples, can provide independent constraints capable of eliminating such a possibility (Oukbir & Blanchard 1992). The RDCS survey (Rosati *et al.* 1998) is currently the X-ray-selected survey with the most extensive redshift data available for distant clusters. The survey, as analyzed by Borgani *et al.* (1999b), is complete within 33 sq deg to limiting 0.5–2 keV X-ray flux  $5 \times 10^{-14}$  erg s $^{-1}$  cm $^{-2}$  and contains 70 clusters with measured redshifts extending to near one.

To explore the compatibility of the octant survey populations with the RDCS sample requires a model for the X-ray luminosity  $L_x$  anticipated from the simulated clusters. As a base model, we assume a mean bolometric  $L_x$ – $T$  relation  $L_x = 2.9 \times 10^{44} (T/6 \text{ keV})^{2.88} h^{-2}$  erg s $^{-1}$  (Arnaud & Evrard 1999) that is assumed not to evolve with redshift (Mushotzky & Scharf 1997; Henry 2000; Fairley *et al.* 2000). To account for the fact that the  $L_x$ – $T$  mapping is not one-to-one, we add a uniformly distributed scatter of  $\pm 0.4$  in  $\log_{10}(L_x)$ . Fluxes in an observed 0.5–2 keV X-ray band are derived from a `mekal` spectral synthesis code assuming 0.3 solar metallicity. Applying a  $5 \times 10^{-14}$  erg s $^{-1}$  cm $^{-2}$  flux cut, excluding  $z < 0.05$  clusters, and scaling the PO and NO simulated cluster surveys to 33 sq deg area leads to predictions shown as the solid lines in Figure 14. Under these economical assumptions of ICM evolution, the  $\Lambda$ CDM model provides an acceptable fit to the observations.

However, this model may be overly simplistic in its treatment of the observed X-ray luminosity from distant clusters. The most distant sources typically are very faint and detected at very low signal-to-noise. One must take care to consider additional sources of X-ray emission that may help push clusters above the survey flux limit. For the purpose of illustration, we consider adding to the base model random additional sources of X-ray luminosity whose influence increases mildly with redshift. These sources may be thought of as contributions from cooling flows or active galaxies embedded within or near the cluster. Specifically, we assume that half of the population has luminosities boosted by an amount drawn from a uniform distribution of amplitude  $\alpha(z)L_x$ , with  $\alpha(z) = 2z$  and  $L_x$  the base luminosity. The linear variation with redshift is intended to account for the increasing difficulty of separating point source contributions from extended emission in fainter clusters. Although possibly extreme, this model raises the zero-point of the  $L_x$ – $T$  relation by only 50% at  $z = 0.5$  relative to the base model. Expectations for RDCS based on this alternative model are shown as dashed lines in Figure 14. The observations straddle the interval defined by the two cosmologies.

Deeper X-ray imaging with *Chandra* and XMM will settle the issue of whether this toy model is too extreme. For now, we note that the good agreement between the RDCS and the economical  $\Lambda$ CDM model predictions may signal that the ICM undergoes relatively simple evolution dominated by gravitational shock heating after an initial, early epoch of preheating (Evrard & Henry 1991; Kaiser 1991; Bower 1997; Cavaliere, Menzi & Tozzi 1999; Balogh, Babul & Patton 1999; Llyod-Davies, Ponman & Cannon 2000;

Bower *et al.* 2001; Bialek, Evrard & Mohr 2001; Tozzi & Norman 2001). The preheated cluster simulations of Bialek *et al.* (2001) produce low redshift scaling relations for X-ray luminosity, isophotal size and ICM mass versus temperature that simultaneously match local observations. They also show little evolution in the  $L_x$ – $T$  relation to  $z \sim 1$ .

## 5.2. Mass-selected samples

Interferometric SZ surveys have been proposed that would survey  $\sim 10$  sq deg of sky per year with sufficient sensitivity to detect all clusters above a total mass limit  $\sim 10^{14} h^{-1} M_\odot$ , nearly independent of redshift (Holder *et al.* 1999; Kneissl *et al.* 2001). The mass limit assumes that the ICM mass fraction does not depend strongly on cluster mass or redshift, an assumption supported by the preheated simulations of Bialek *et al.* (2001). They find that the ICM gas fraction within  $\Delta = 200$  remains a fair representation of the baryon-to-total cosmic ratio:  $f_{\text{ICM}} = (0.92 \pm 0.04) \Omega_b / \Omega_m$  above rest frame temperature  $kT = 4$  keV. In this section, we investigate expectations for SZ surveys assuming that they will be sensitive to a limiting total mass that is independent of redshift.

Maps of mass-limited cluster samples in SDSS-like survey slices were presented in Figure 6 for the default values of  $\sigma_8$ . To illustrate the effect of  $\sigma_8$  variation, we plot clusters in these same spatial regions again in Figure 15, after applying an effective fractional variation in  $\sigma_8$  of +10% ( $\tau$ CDM) and -10% ( $\Lambda$ CDM). Although equation (11) suggests a simple shift in mass threshold to mimic a change in  $\sigma_8$ , the mass dependence of  $\alpha'(M)$  (Figure 12) introduces cumbersome non-linearity into the shift. We adopt instead an effectively equivalent procedure that adjusts both masses  $M$  and number densities  $n(M)$  in the HV cluster catalogs by amounts

$$M' = e^\mu M, \\ n(M') d \ln M' = e^{-\mu} n(M) d \ln M \quad (15)$$

with

$$\mu = \frac{\ln(1 + \Delta\sigma_8/\sigma_8)}{\langle \alpha_{\text{eff}} \rangle} \quad (16)$$

and  $\langle \alpha_{\text{eff}} \rangle = 0.25$ . Tests of these transformations using the Jenkins mass function verify their accuracy to better than 10% in number for masses  $10^{13.7} - 10^{15.3} h^{-1} M_\odot$  and variations of power spectrum normalization within the 90% confidence region  $|\Delta\sigma_8/\sigma_8| \leq 0.16$ . The practical value of these simple transformations is in allowing the discrete simulation output to represent a family of models covering a range of normalizations  $\sigma_8$ .

In Figure 15, the cluster populations expected in the two cosmologies are now much more similar. Unlike Figure 6, the overall counts above  $10^{14} h^{-1} M_\odot$  in the 3 degree slice are now nearly identical — 1696 for  $\tau$ CDM compared to 1843 for  $\Lambda$ CDM. However, their redshift distributions remain different; the  $\tau$ CDM clusters concentrate at lower redshifts while the  $\Lambda$ CDM clusters are more uniformly distributed (Oukbir & Blanchard 1992).

Figures 6 and 15 suggest that a redshift statistic, such as the sample median, will be superior to counts as a means to constrain cosmology. Motivated by the aforementioned planned SZ surveys, we perform a specific investigation

of expectations for a random 10 sq deg survey complete above a mass-limit  $M_{200} = 10^{14} h^{-1} M_{\odot}$ . We sample clusters in 3000 randomly oriented, square fields of 10 sq deg area, equally divided between the PO and NO surveys and chosen to avoid survey boundaries. We use the transformations in equation (15) to define the cluster population at values of  $\sigma_8$  different from the default. To drive the models in directions that minimize their differences, we increase  $\sigma_8$  in the  $\tau$ CDM model and decrease it in the  $\Lambda$ CDM case.

The distributions of counts at all redshifts ( $z < 1.25$ ), counts at high redshift ( $0.8 < z < 1.25$ ) and the median redshift for clusters above the survey mass limit derived from the 3000 random 10 sq deg samples are presented in Figure 16. At the default values of  $\sigma_8$  (left column), the distributions of number expected either at all redshifts  $z < 1.25$  (bottom row) or at high redshift (middle row) would allow unambiguous discrimination between the models using a single 10 sq deg field. At high redshift, the  $\Lambda$ CDM model predicts, on average, a factor 15 more clusters than  $\tau$ CDM. Overall, the mean counts in 10 sq deg are 117 and 45, respectively. Biasing  $\sigma_8$  by 10% in the chosen directions (middle column) produces essentially identical expectations for the overall cluster yield, with both models expecting  $72 \pm 12$  clusters per field. At high redshift, the ability to discriminate is weakened. For a 16% bias (right column), the sense of the overall counts are reversed, with the  $\tau$ CDM model having a 60% larger yield, on average, than  $\Lambda$ CDM. The high redshift count distributions of the models possess considerable overlap.

In contrast to the count behavior, the distributions of sample median redshift  $z_{\text{med}}$  are extremely stable to variations in  $\sigma_8$ . The 95-th percentile value of  $z_{\text{med}}$  for  $\tau$ CDM moves from 0.498 to 0.528 at 0, 10% and 16% bias. As a measure of discrimination we quote the power (Sachs 1982), defined as the probability of rejecting  $\tau$ CDM at the chosen level (95%) of significance given  $\Lambda$ CDM as the true model. Measuring the power by integrating the  $\Lambda$ CDM distributions of  $z_{\text{med}}$  above the 95-th percentile  $\tau$ CDM value, results in power of 99.9%, 98.8% and 94.8%. These power measures, and others calculated in a similar manner for the counts, are listed in corresponding panels of Figure 16. High redshift counts lose power to discriminate between the models as the applied bias on  $\sigma_8$  is increased.

Of course, the large shift in the expected counts as  $\sigma_8$  is varied provides an appropriate lever arm to use for placing firmer constraints on this parameter with SZ surveys. Holder, Haiman and Mohr (2001) estimate that a survey of the type assumed here could, with complete redshift information and assuming perfect knowledge of the relation between SZ signal and cluster mass, constrain  $\sigma_8$  at the 3–5% level.

### 5.3. Very distant clusters

*Chandra* X-ray Observatory detections of extended X-ray emission from three clusters at  $z > 1$  have recently been reported. Stanford *et al.* (2001) report detection of hot ICM in a pair of RDCS-selected clusters separated by only 4 arcmin on the sky and 0.01 in redshift, RX J0848+4453 at  $z = 1.27$  and RX J0849+4452 at  $z = 1.26$  (Stanford *et al.* 1997; Rosati *et al.* 1999). RX J0849+4452 appears to have a complex morphology and a cool temperature  $kT = 1.6_{-0.6}^{+0.8}$  keV while

RX J0848+4453 appears to be a relaxed system with higher temperature  $kT = 5.8_{-1.7}^{+2.8}$  keV. In addition to these systems, Fabian *et al.* (2001) present *Chandra* evidence for extended ICM emission at temperature  $kT = 5.0_{-1.5}^{+2.6}$  keV around the radio galaxy 3C294 at  $z = 1.786$ . Quoted errors in these temperature estimates are 68% confidence values.

From the temperature–mass relation calibrated by the local temperature function sample in §4 and assuming a non-evolving  $\beta$ , we can estimate the masses of these clusters. Results for  $\Lambda$ CDM ( $\tau$ CDM) are  $M_{200} = 3.1$  (2.7)  $\times 10^{14} h^{-1} M_{\odot}$  and  $4.4$  (3.9)  $\times 10^{13} h^{-1} M_{\odot}$  for RX J0848+4453 and RX J0849+4452, respectively, and  $M_{200} = 1.9$  (1.6)  $\times 10^{14} h^{-1} M_{\odot}$  for 3C294. The likelihood of finding such clusters can be computed by integrating the Jenkins mass in the manner used to generate the expectations  $N(> M_{200}, > z)$  shown in Figure 8. Following the SZ counts analysis of the preceding section, it is important to take into account uncertainty in the fluctuation normalization  $\sigma_8$ . We therefore compute counts using the upper and lower 90% confidence values of  $\sigma_8$  and plot the resultant range in Figure 17. We show only expectations for counts above  $10^{14}$  and  $10^{15} h^{-1} M_{\odot}$ , as the allowed range in surface density can be quite large — factors of 30 or more at  $z \gtrsim 1$ .

### 5.4. Sky surface density characteristics

Rather than attempt to place the observations directly on the cumulative count figure, we take the approach of examining a statistic that emphasizes physical measurables (mass and temperature) and their attendant uncertainties.

The statistics we consider are sky surface density characteristics, defined as the mass  $M_{N'}(z)$  and temperature  $T_{N'}(z)$  at which the differential sky surface density  $N'(z) \equiv dN/dz$  of rank-ordered clusters at redshift  $z$  takes on fixed values. The mass scale  $M_{N'}(z)$  is defined by the relation

$$N'(z) = (1/\Omega_{\text{surv}}) \int_{M_{N'}(z)}^{\infty} d \ln M \, n(M, z) \, dV/dz \quad (17)$$

where  $\Omega_{\text{surv}}$  is the appropriate survey sky area. The characteristic temperature is defined in a similar manner. As a practical approximation to the pure differential, we employ counts in redshift bins of width 0.1 to derive this statistic from the HV sky survey data.

Figure 18 shows the redshift behavior of the sky surface density characteristic (SSDC) mass and temperature for the  $\Lambda$ CDM model. Filled points are values based on the combined octant survey populations. Solid lines are predictions from the Jenkins mass function, derived by computing equation (17) using equation (9) for  $n_{\text{JMF}}(M, z)$  and integrating in bins of width 0.1 in redshift. Sky surface density thresholds  $dN/dz$  vary by factors of 10 from 0.001 to 10 per sq deg per unit redshift, as labeled. Open circles show results for the SSDC at 0.01 per sq deg per unit redshift extending to  $z \sim 3$  using the  $16^{\circ} \times 76^{\circ}$  extension to the PO survey. Thick dashed lines in each panel show the limiting resolved mass of  $5 \times 10^{13} h^{-1} M_{\odot}$  (22 particles) and the corresponding limiting resolved virial temperature. The good agreement between the Jenkins model and the discrete cluster sample measurements is to be expected from the results of Figure 7; the POX extension data verify the utility of the model to  $z \sim 3$ .

The vertical bar in each panel of Figure 18 shows the 90% uncertainty range in the local calibration of each quantity;  $\pm 0.26$  in  $\ln T$  (mostly) from cosmic variance and  $\pm 0.60$  in  $\ln M$  from combined cosmic variance and  $M-T$  calibration uncertainty. The HV simulation and Jenkins model results for the SSDC measures are allowed to range vertically by these amounts in Figure 18. The narrow spacings between  $M_{N'}(z)$  and  $kT_{N'}(z)$  contours reflect the steepness of the cumulative counts at fixed redshift; topographically speaking, the terrain of the counts is steep in the mass and temperature directions. The calibration errors in these measures translate into large ranges of allowed sky surface densities for a given mass or temperature at a particular redshift. This is another perspective on the range of allowed cumulative counts shown in Figure 17.

Although steep in the temperature direction, the contours in the lower panel of Figure 18 are remarkably flat in the redshift direction. Over the entire redshift interval  $0.1 < z < 1.5$ , the JMF expectations for the SSDC temperature at 0.01 per sq deg per unit redshift lie in a narrow range between 8 and 10 keV. In the  $\Lambda$ CDM model, distant, hot cluster should be as abundant on the sky as those nearby.

Temperatures of the aforementioned observed distant clusters are plotted in the lower panel of Figure 18 as open triangles (the RX clusters) and open square (3C294). Temperature uncertainties at 90% confidence are shown, assuming Gaussian statistics to convert  $1\sigma$  errors. The central values of the hotter pair are consistent with a sky surface density of 1 per 10 sq deg per unit redshift, but within the temperature measurement uncertainties, these objects could be up to a factor 100 more common or a factor  $\sim 1000$  more rare. The lower temperature system at  $z=1.27$  is consistent with a surface density of several per sq deg per unit redshift.

Figure 19 shows that the  $\tau$ CDM model is less able to accommodate the existence of these  $z > 1$  clusters. The central temperatures correspond to surface densities of 1 per 1000 sq deg per unit redshift, a factor 100 times more dilute than the  $\Lambda$ CDM values. Given that only 40 such clusters would be expected on the whole sky between redshifts one and two, it would be remarkable that two would already be identified by these observations.

At the most dilute sky surface density plotted in these figures, each filled circle represents the hottest or most massive cluster within its 0.1-wide redshift bin. Even at this highest rank-order, the variance in the discrete sample SSDC values remains remarkably small. An exception is the unusual  $\Lambda$ CDM at  $z=1.04$ . This monster lies nearly a factor two above the Jenkins model expectations and its deviation is extreme compared to that displayed by values at the same source density and other redshifts. We note that its expected temperature of 21 keV exceeds that of the hottest known cluster 1E 0657-56 at  $z=0.296$ , with  $kT=17.4 \pm 2.5$  keV (Tucker *et al.* 1998). This cluster is the asterisk in Figures 18 and 19.

As the hottest known cluster, it is natural to expect 1E 0657-56 to lie at the extreme end of the surface density distribution in the redshift range  $0.2 - 0.3$ . That is indeed the outcome of comparing its location to  $\Lambda$ CDM expectations in Figure 18. For the case of  $\tau$ CDM, its existence is more troublesome, but given the combination of  $T$  calibration uncertainty and scatter demonstrated by

the first-ranked values of the discrete sample, this system is consistent at the  $\sim 2\sigma$  level with the expectations of Figure 19. A similar statement of significance can be made for the comparably hot and more distant cluster RX J1347-1145, with  $kT=14.48^{+1.76}_{-1.46}$  keV (Ettori, Allen & Fabian 2001) at  $z=0.451$ . We therefore disagree with the interpretation of Ettori *et al.* (2001) that the existence of RX J1347-1145 alone can be used to place an upper limit on the matter density parameter  $\Omega_m < 0.5$ .

To summarize, interpretation of distant cluster counts is complicated by uncertainty in  $\sigma_8$ , variation of which can lead to large factor changes in yield, as well as uncertainty due to possible evolution in  $\beta$  and other aspects of astrophysical evolution. If a constant  $\beta$  assumption is valid for  $\Lambda$ CDM, then  $\sim 8$  keV clusters at  $z=1.2 - 1.3$  should be as numerous on the sky as those lying at  $z=0.1 - 0.2$ .

## 6. SUMMARY OF $\Lambda$ CDM EXPECTATIONS

Given the increasing likelihood that the  $\Lambda$ CDM model is an accurate representation of our universe (Pryke *et al.* 2001; Netterfield *et al.* 2001), we provide here a brief summary and discussion of the characteristics of its cluster population.

*Coma-mass systems.* The population of clusters with  $M_{200}$  in excess of  $10^{15} h^{-1} M_\odot$  is potentially numerous, but not overwhelmingly so. With the default  $\sigma_8=0.9$ , 400 clusters are expected on the whole sky (Figure 8), but that number ranges between 40 and 2000 as  $\sigma_8$  is varied within its 90% confidence limits (Figure 17). The median redshift of this sample is expected to be  $z_{\text{med}}=0.48$ , nearly independent of  $\sigma_8$ . Detection of Coma equivalents at  $z>1$  in excess of .003 per sq deg ( $\sim 120$  across the sky) would rule out  $\Lambda$ CDM at 95% confidence. A complete sample of these objects could be obtained with an all-sky X-ray imaging survey only moderately more sensitive than the RASS. Such a survey would be unique in being the first to be *universally complete*, meaning complete in identifying *all* members of a class of astrophysical objects within the finite volume of our past light-cone.

*Hot X-ray clusters.* A characteristic feature of the  $\Lambda$ CDM model is that the hottest clusters populate the sky at nearly fixed surface density over a broad redshift interval (Figure 18). This implies a testable prediction of a nearly flat redshift distribution, within  $z \simeq 0.2 - 1$ , for a temperature-limited sample identified in a fixed angular survey area. Within the 10,000 sq deg SDSS area, one 8 keV cluster is expected to lie beyond  $z=2$  for  $\sigma_8=0.9$ .

*Clusters at  $z \sim 3$ .* Looking to higher redshifts, clusters with  $M_{200} > 10^{14} h^{-1} M_\odot$  and rest frame  $kT > 4$  keV (apparent  $kT \gtrsim 1$  keV) should exist at the level of one cluster per 100 sq deg per unit redshift under the default  $\sigma_8$  and  $\beta$  normalizations (Figure 18). Of order one hundred such clusters are to be expected within the SDSS survey area in the redshift interval  $2.5 - 3.5$ . Of order ten clusters will have rest frame  $kT > 5$  keV and  $z > 3$ . The vicinity of bright quasars may be a natural place to search for these systems. Verification of a hot ICM at these redshifts would benefit from the large collecting area of the planned Constellation-X Observatory.

*Clusters at  $z \lesssim 0.5$ .* The SDSS and 2dF optical surveys will provide large numbers of clusters selected in redshift-space and extending to redshifts nearing  $z=0.5$ . These samples offer the opportunity to place more stringent con-

straints on  $\sigma_8$ , but only if a number of systematic effects, such as biases in the selection process and the mapping between measured properties (optical richness or velocity dispersion) and underlying cluster mass  $M$ , can be carefully calibrated. Such systematic effects can be profitably studied by combining semi-analytic models of galaxy formation with N-body models of dark matter halo evolution (*e.g.*, Springel *et al.* 2001). An X-ray imaging survey to bolometric flux  $10^{-14}$  erg s $^{-1}$  cm $^{-2}$ , capable of identifying all clusters with  $M_{200} > 10^{14} h^{-1} M_\odot$  within  $z = 0.4$  (assuming a non-evolving  $L_X-T$  relation), would provide the ability to separate truly deep potential wells from redshift space superpositions of smaller systems (Frenk *et al.* 1990).

*ICM temperature evolution.* In predicting that the redshift distribution of hot clusters at fixed sky surface density is flat over observationally accessible redshifts, we have implicitly assumed that the X-ray temperature and mass follow the virial relation  $T \propto (h(z)M_{200})^{2/3}$ . It is important to pursue high resolution imaging and spectroscopy of known high redshift clusters with *Chandra* and XMM in order to test whether more complex heating and cooling processes may be occurring, particularly at high redshift. Such processes would affect attempts to determine the geometry of the universe through the X-ray size-temperature relation (Mohr & Evrard 1997; Mohr *et al.* 2000). The cleanest approach to calibrate the  $M-T$  relation empirically remains weak gravitational lensing (*e.g.*, Clowe *et al.* 2000), but precise mass estimates are hampered by small sample sizes, the intrinsically weak signal and, for high redshift clusters, uncertainty in the redshift distribution of lensed galaxies.

## 7. CONCLUSIONS

We present analysis of a pair of giga-particle simulations designed to explore the emergence of the galaxy cluster population in large cosmic volumes of flat world models dominated by matter energy density ( $\tau$ CDM) and a cosmological constant ( $\Lambda$ CDM). Besides shear scale, these Hubble Volume simulations are unique in their production of sky survey catalogs that map structure of the dominant dark matter component over large solid angles and to depths  $z \simeq 1.5$  and beyond. Application of a spherical overdensity (SO) cluster finding algorithm to the sky survey and fixed epoch simulation output results in discrete samples of millions of clusters above the mass scale of galaxy groups ( $5 \times 10^{13} h^{-1} M_\odot$ ). These samples form the basis of a number of studies; we focus here on precise calibration of the mass function and on quantification of systematic uncertainties in cosmological parameter determination caused, in particular, by uncertainty in our knowledge of absolute mass and temperature scales. A summary of our principal findings is as follows.

- We calibrate the SO(200) mass function to the Jenkins form with resulting statistical precision of better than 3% in number for masses between  $10^{13.5}$  and  $10^{15.3} h^{-1} M_\odot$ . A preliminary estimate of the overall theoretical uncertainty in this calibration is approximately 20%.
- Large-scale variations in the matter density cause the number of nearby ( $z \lesssim 0.1$ ) clusters to vary sys-

tematically about the global mean. Based on subsampling the full simulation to mimic a local sample of 38 observed X-ray cluster temperatures, we show that such cosmic variance adds systematic uncertainty of  $\sim 6\%$  to determinations of the power spectrum normalization  $\sigma_8$ . Assuming that, in the mean, cluster masses are calibrated to no better than 20% absolute accuracy, we estimate the 90% confidence overall systematic uncertainty in  $\sigma_8$  to be 16%.

- Based on the Jenkins form for the mass function, we derive transformations of the discrete cluster sample that mimic variation in  $\sigma_8$ . A similar analysis, coupled with an assumption of the NFW form for mean internal density profiles of clusters, leads to a prescription to transform the mass function fit parameters presented here to threshold values other than 200.
- Using the above transformations to explore the sensitivity of survey yields to  $\sigma_8$  uncertainty, we show that counts of clusters alone are insufficient to place tight constraints on cosmological models. The redshift distribution adds critical information; the median redshift of clusters more massive than  $10^{14} h^{-1} M_\odot$  in a single 10 sq deg field of a  $\Lambda$ CDM cosmology can rule out  $\tau$ CDM at a minimum of 95% confidence. In likelihood terms,  $p(\mathcal{C} | z_{\text{med}})$  is sharply peaked; no single measure of  $z_{\text{med}}$  would result in the two models being both equally likely and probable with respect to the maximum likelihood.
- The  $\Lambda$ CDM model requires a minimal set of assumptions for intracluster gas evolution to be compatible with high redshift X-ray observations of the EMSS and RDCS surveys. The  $\tau$ CDM model requires modest evolutionary adjustments for the intracluster medium that are not yet formally ruled out. However, the  $\tau$ CDM model cannot explain the baryon fraction in clusters while remaining compatible with cosmic light-element nucleosynthesis (White *et al.* 1993; Evrard 1997).
- We introduce the statistic of sky surface density characteristic (SSDC) mass and temperature in order to more naturally account for observational and theoretical uncertainties in measured scales. The  $\Lambda$ CDM model predicts flat redshift behavior in the SSDC temperature; a randomly chosen 8 keV cluster on the sky is nearly equally likely to lie at any redshift in the interval  $z \in 0.2 - 1.2$ .
- With  $\sigma_8 = 0.9$ , the  $\Lambda$ CDM model predicts roughly 400 Coma-mass ( $10^{15} h^{-1} M_\odot$ ) clusters across the sky at all redshifts, with the most distant lying just beyond  $z = 1$ . Pushing  $\sigma_8$  to its 95% confidence upper limit, the  $\Lambda$ CDM model could accommodate up to  $\sim 120$  Coma equivalents on the sky at  $z > 1$ .
- The existence in a single realization of the Hubble Volume of an extremely rare event — the  $z = 1.04$  ‘monster’ with  $M_{200} = 2 \times 10^{15} h^{-1} M_\odot$  and expected  $kT = 21$  keV — serves as a cautionary reminder of the role of serendipity in studies of sample extrema.

To improve constraints on  $\sigma_8$  and  $\Omega_m$ , larger and deeper cluster samples with accurate determinations of temperature or mass are needed. The developing 2dF and SDSS surveys will provide large numbers of clusters with galaxy velocity dispersion  $\sigma_{\text{gal}}$  serving as a temperature measure and optical richness  $\mathcal{L}$  serving as a surrogate for mass. Gravitational lensing mass estimates will also be possible for co-added ensembles of clusters (Sheldon *et al.* 2001). Extracting cosmological information from these data will require likelihoods such as  $p(\sigma_v | \sigma_{\text{gal}})$  or  $p(M | \mathcal{L})$ . The challenge to the theoretical community will be to model these likelihoods at a level of precision warranted by the large data sets. Almost certainly, the theoretical uncertainty associated with this aspect of the modeling will dominate statistical errors, since samples of many thousands, perhaps tens of thousands, of groups and clusters will be available in the complete 2dF and SDSS surveys. An alternative path will be to impose external constraints on cosmological parameters and then derive constraints on these ‘astrophysical’ aspects empirically.

Valuable complementary information is available at X-ray wavelengths. An X-ray imaging survey reaching to limiting flux  $\sim 3 \times 10^{-14} \text{ erg s}^{-1} \text{ cm}^{-2}$  in the  $0.5 - 6 \text{ keV}$  band would be capable of detecting a cluster with  $6 \text{ keV}$  rest frame temperature to  $z = 1$  in either of the cosmologies studied here, assuming a non-evolving  $L_X - T$  relation. The redshift distribution of such a sample would be a powerful cosmological diagnostic, as long as astrophysical evolution of the ICM could be sufficiently well constrained. A program of deep pointed observations with *Chandra* and

XMM (to constrain the astrophysical evolution), coupled with a deep X-ray imaging survey covering a significant portion of the SDSS area (to identify a large cluster population in redshift space) would be a powerful combination. SZ surveys over large solid angle with bolometer arrays could play a similar role to an X-ray imaging mission, and interferometric arrays will probe to smaller masses and higher redshifts than can be achieved by any current search techniques. Ultimately, the combination of *all* these approaches, along with deep, optical imaging and spectroscopy, will allow determinations of cosmological parameters to be made not only more precise, by shear statistical weight, but also be made more accurate by improving our understanding of the astrophysical processes that govern the evolution of cluster components.

The cluster samples described in this paper are available at <http://astro.physics.lsa.umich.edu/HV/tables.htm>.

This work was funded by the PPARC in the UK, the Max-Planck Society in Germany, NSERC in Canada, NASA and NSF in the US, and NATO in all the countries involved. Some of this work was carried out as part of the EU Network for Galaxy Formation and Evolution. CSF acknowledges a Leverhulme Research Fellowship. We thank the staff of the Rechenzentrum Garching for outstanding computational support. AEE acknowledges support from NSF AST-9803199 and NASA NAG5-7108, clarifying conversations with A. Blanchard and J. Bartlett, and the benefits of the Scientific Visitor Program at Carnegie Observatories in Pasadena.

## REFERENCES

Arnaud, M. & Evrard, A.E. 1999, MNRAS , 305, 631.  
 Annis, J., Garzoglio, G., Kent, S., Kim, R., Goto, T. & the SDSS Collaboration 2001, BAAS, 198, 2601.  
 Bahcall, N.A. & Fan, X., 1998, ApJ , 504, 1.  
 Bahcall, N.A., Fan, X. & Cen, R. 1997, ApJ , 485, L53.  
 Balogh M.L., Babul A., Patton D.R., 1999, MNRAS , 307, 463.  
 Barbosa, D., Bartlett, J., Blanchard, A. & Oukbir, J 1996, A&A , 314, 13.  
 Bialek, J., Evrard, A.E. & Mohr, J.J. 2001, ApJ , in press, astro-ph/0010584.  
 Blanchard, A. & Bartlett, J.G. 1998, A&A , 332, L49.  
 Blanchard, A., Sadat, R., Bartlett, J. & Le Dour, M. 2000, A&A , 362, 809.  
 Bode, P., Bahcall, N.A., Ford, E.B., & Ostriker, J.P. 2001, ApJ , 551, 15.  
 Böhringer, H., Schuecker, P., Guzzo, L., Collins, C.A., Voges, W., Schindler, S., Neumann, D.M., Crude, R.G., De Grandi, S., Chincarini, G., Edge, A.C., MacGillivray, H.T. & Shaver, P. 2001, A&A , 369, 826.  
 Bond, J. R. & Efstathiou, G., 1984, ApJ , 285, L45.  
 Bond, J.R., Cole, S., Efstathiou, G. & Kaiser, N. 1991, ApJ , 379, 440.  
 Borgani, S., Girardi, M., Carlberg, R.G., Yee, H.K.C., Ellingson, E. 1999a, ApJ , 527, 561.  
 Borgani, S., Rosati, P., Tozzi, P., Norman, C. 1999, ApJ , 517, 40.  
 Bower, R.G. 1997, MNRAS , 288, 355.  
 Bower, R.G., Benson, A.J., Lacey C.G., Baugh, C.M., Cole, S. & Frenk, C.S. 2001, MNRAS , 325, 497.  
 Bryan, G.L. & Norman, M.L. 1998, ApJ , 495, 80.  
 Bullock, J.S., Kolat, T.S., Sigad, Y., Somerville, R.S., Kravtsov, A.V., Klypin, A.A., Primack, J.R. & Dekel, A. 2001, MNRAS , 321, 559.  
 Carlberg, R.G., Yee, H.K.C., Ellingson, E. 1997, ApJ , 478, 462.  
 Casertano, P. & Hut, P. 1985, ApJ , 298, 80.  
 Cavaliere, A. & Fusco-Femiano, R. 1976, A&A , 49, 137.  
 Cavaliere A., Menci N. & Tozzi P., 1999, MNRAS , 308, 599.  
 Clowe, D., Luppino, G.A., Kaiser, N. & Gioia, I.M. 2000, ApJ , 539, 540.  
 Colberg, J., White, S.D.M., Yoshida, N., MacFarland, T., Jenkins, A., Frenk, C.S., Pearce, F.R., Evrard, A.E., Couchman, H.M.P., Efstathiou, G., Peacock, J. & Thomas, P. 2000, MNRAS , 319, 209.  
 Colombi, S., Szapudi, I., Jenkins, A. & Colberg, J. 2000, MNRAS , 313, 711.  
 Dalton, G.B., Maddox, S.J., Sutherland, W.J. & Efstathiou, G. 1997, MNRAS , 289, 263.  
 David, L.P., Nulsen, P.E.J., McNamara, B.R., Forman, W., Jones, C., Ponman, T., Robertson, B. & Wise, M. 2001, submitted to ApJ , astro-ph/0010224.  
 de Grandi, S., Böhringer, H., Guzzo, L. *et al.* 1999, ApJ , 514, 148.  
 De Propris, R., Couch, W.J. & the 2dFGRS Team, astro-ph/0010498.  
 Donahue, M., Voit, G.M., Gioia, I.M., Luppino, G., Hughes, J.P. & Stocke, J.T. 1998, ApJ , 502, 550.  
 Ebeling, H., Edge, A. C., Bhringer, H., *et al.* 1998, MNRAS, 301, 881.  
 Ebeling, H., Edge, A. C. & Henry, J.P. 2001, submitted, astro-ph/0009101.  
 Eke, V.R., Cole, S. & Frenk, C.S., MNRAS , 282, 263.  
 Eke, V.R., Cole, S., Frenk, C.S. & Henry, J.P., MNRAS , 298, 1145.  
 Ettori, S., Allen, S.W., Fabian, A.C. 2001, MNRAS , 322, 187.  
 Evrard, A.E. 1990, ApJ , 363, 34.  
 Evrard, A.E. 1997, MNRAS , 292, 289.  
 Evrard A.E. & Henry J.P., 1991, ApJ , 383, 95.  
 Evrard, A.E., Metzler, C. & Navarro, J.F. 1996, ApJ , 469, 494.  
 Fabian, A.C., Crawford, C.S., Ettori, S. & Sanders, J.S. 2001, MNRAS , 322, 11.  
 Fairley B.W., Jones L.R., Scharf C., Ebeling H., Perlman E., Horner D., Wegner G. & Malkan M., 2000, MNRAS , 315, 669.  
 Fan, X., Bahcall, N.A. & Cen, R. 1997, ApJ , 490, 123.  
 Finoguenov, A., Reiprich, T.H., & Böhringer, H. 2001, A&A , 368, 749.  
 Fischer, P. *et al.* 2000, AJ, 120, 1198.  
 Frenk, C. S., White, S. D. M., Efstathiou, G. & Davis, M. 1990, ApJ , 327, 507.  
 Frenk, C. S., White, S. D. M., Efstathiou, G. & Davis, M. 1990, ApJ , 351, 10.  
 Frenk, C. S., White, S. D. M., Bode, P., *et al.* 1999, ApJ , 525, 554.

Gal, R.R., de Carvalho, R.R., Odewahn, S.C., Djorgovski, S.G. & Magoniner, V.E. 2000, AJ, 119, 12.

Gioia, I.M. & Luppino, G.A. 1994, ApJS, 94, 583.

Gladders, M.D. & Yee, H.K.C. 2000, AJ, 120, 2148.

Gonzalez, A.H., Zaritsky, D., Dalcanton, J.J. & Nelson, A. 2001, ApJS, in press, astro-ph/0106055.

Governato, F., Babul, A., Quinn, T., Tozzi, P., Baugh, C.M., Katz, N. & Lake, G., 1999, MNRAS, 307, 949.

Henry, J.P. 2000 ApJ , 534, 565.

Henry, J.P. & Arnaud, K.A. 1991, ApJ , 372, 410.

Henry, J.P., Gioia, I.M., Maccacaro, T., Morris, S.L., Stocke, J.T. & Wolter, A. 1992, ApJ , 386, 408.

Hjorth, J., Oukbir, J. & van Kampen, E 1998, MNRAS , 298, 1.

Holder, G.P., Haiman, Z. & Mohr, J. 2001, submitted to ApJ , astro-ph/0105396.

Holder, G.P., Mohr, J.J., Carlstrom, J.E., Evrard, A.E., Leitch, E.M. 2000, ApJ , 544, 629.

Horner, D.J., Mushotzky, R.F. & Scharf, C.A. 1999, ApJ , 520, 78.

Jenkins, A., Frenk, C.S., White, S.D.M., Colberg, J.M., Cole, S., Evrard, A.E., Couchman, H.M.P., Yoshida, N. 2001, MNRAS , 321, 372 (J01).

Jing, Y.P. 2000, ApJ , 535, 30.

Kaiser, N., 1991, ApJ , 383, 104.

Kay, S.T., Liddle, A.R. & Thomas, P.A. 2001, submitted to MNRAS , astro-ph/0102352.

Kerscher, M., Szapudi, I. & Szalay, A.S. 2000, ApJ , 535, L13.

Kepner, J., Fan, X., Bahcall, N., Gunn, J., Lupton, R., Xu, G. 1999 ApJ , 517, 78.

Kitayama, T. & Suto, Y. 1997, ApJ , 490, 557.

Kneissl, R., Jones, M.E., Saunders, R., Eke, V.R., Lasenby, A.N., Grainge, K. & Cotter, G. 2001, submitted to MNRAS , astro-ph/0103042.

Lacey, C. & Cole, S., 1994, MNRAS, 271, 676.

Lahav, O., Rees, M.J., Lilje, P.B. & Primack, J.R. 1991, MNRAS , 251, L128.

Lee, J. & Shandarin, S. 1999, ApJ , 517, 5.

Lilje, P.B. 1992, ApJ , 386, L33.

Lloyd-Davies E.J., Ponman T.J. & Cannon D.B., 2000, MNRAS , 315, 689.

Luppino, G. & Kaiser, N. 1997, ApJ , 475, 20.

MacFarland, T., Couchman, H.M.P., Pearce, F.R., & Pichlmeier, J. 1998, NewA, 3, 687.

Markevitch, M. 1998, ApJ , 504, 27.

Mathiesen, B.F. & Evrard, A.E. 2001, ApJ , 546, 100.

McNamara, B.R., Wise, M.W., David, L.P., Nulsen, P.E.J. & Sarazin, C.L. 2001, in Constructing the Universe with Clusters of Galaxies, Paris, July 2000, astro-ph/0012331.

Netterfield, C.B. *et al.* 2001, astro-ph/0104460.

Metzler, C.A., White, M., Loken, C. 2001, ApJ , 547, 560.

Mohr, J.J., Mathiesen, B. & Evrard, A.E. 1999, ApJ , 517, 627.

Mohr, J.J., Reese, E.D., Ellingson, E., Lewis, A.D. & Evrard, A.E. 2000, ApJ , 544, 109.

Moore, B., Governato, F., Quinn, T., Stadel, J. & Lake, G. 1998, ApJ , 499, L5.

Mushotzky, R. & Scharf, C.A. 1997, ApJ 482, L13.

Navarro, J.F., Frenk, C.S. & White, S.D.M. 1996, ApJ , 462, 563.

Navarro, J.F., Frenk, C.S. & White, S.D.M. 1996, ApJ , 490, 493.

Nevalainen, J., Markevitch, M. & Forman, W. 1999, ApJ , 536, 73.

Nichol, R. *et al.* 2001, to appear in Proceedings of MPA/MPE/ESO Conference "Mining the Sky", astro-ph/0011557.

Ostrander, E.J., Nichol, R.C., Ratnatunga, K.U. & Griffiths, R.E. 1998, AJ, 116, 2644.

Oukbir, J. & Blanchard, A. 1992, A&A , 262, L21.

Outram, P.J., Hoyle, F., Shanks, T., Boyle, B.J., Croom, S.M., Loaring, N.S., Miller, L. & Smith, R.J. 2001, submitted to MNRAS , astro-ph/0106012.

Padilla, N.D. & Baugh, C.M. 2001, submitted to MNRAS , astro-ph/0104313.

Park, C. & Gott, J.R. 1991, ApJ , 378, 457.

Pearce, F.R. & Couchman, H.M.P. 1997, NewA, 2, 411.

Pen, U.-L. 1998, ApJ , 498, 60.

Pierpaoli, E., Scott, D. & White, M. 2001, MNRAS , in press, astro-ph/0010039 (PSW).

Postman, M., Lubin, L., Gunn, J.E., Oke, J.B., Hoessel, J.G., Schneider, D.P. & Christensen, J.A. 1996, AJ, 111, 615.

Press, W.H. & Schechter, P. 1974, ApJ 187, 425.

Prycke, C., Halverson, N.W., Leitch, E.M., Kovac, J., Carlstrom, J.E., Holzapfel, W.L. & Dragovan, M. 2001, submitted to ApJ , astro-ph/0104490.

Romer, A.K., Nichol, R.C., Holden, B.P., Ulmer, M.P., Pildis, R.A., Merrelli, A.J., Adami, C., Burke, D.J., Collins, C.A., Metevier, A.J., Kron, R.G. & Commons, K. 2000, ApJS, 126, 209.

Romer, A.K., Viana, P.T.P., Liddle, A.R., Mann, R.G. 2001, ApJ , 547, 594.

Rosati, P., Della Ceca, R., Norman, C. & Giacconi, R. 1998, ApJ , 492, 21L.

Sachs, L. 1982, Applied Statistics, New York: Springer Verlag.

Sadat, R., Blanchard, A. & Oukbir, J. 1998, A&A , 329, 21.

Scharf, C.A., Jones, L.R., Ebeling, H., Perlman, E., Malkan, M. & Wegner, G. 1997, ApJ , 477, 79.

Scodellaggio, M. *et al.* 1999, A&AS, 137, 83.

Seljak, U. & Zaldarriaga, M. 1996, ApJ , 469, 437.

Sheth, R. K. & Tormen, G. 1999, MNRAS, 308, 119.

Smith, D.R., Bernstein, G.M., Fischer, P. & Jarvis, M. 2001, ApJ , 551, 643.

Springel, V., White, S.D.M., Tormen, G. & Kauffmann, G. 2000, submitted to MNRAS , astro-ph/0012055.

Stanford, S. A., Elston, R., Eisenhardt, P., Spinrad, H., Stern, D., & Dey, A. 1997, AJ, 114, 2232.

Stanford, S.A., Holden, B., Rosati, P., Tozzi, P., Borgani, S., Eisenhardt, P.R. & Spinrad, H. 2001, ApJ , 552, 504.

Sunyaev, R. & Zel'dovich, Y.B. 1972, Comments Astrophys. Space Phys. 4, 173.

Szapudi, I., Colombi, S., Jenkins, A. & Colberg, J. 2000, MNRAS , 313, 725.

Thomas, P.A., Muanwong, O., Pearce, F.R., Couchman, H.M.P., Edge, A.C., Jenkins, A. & Onuora, L. 2001, MNRAS , 324, 450.

Tran, K.-V.H., Kelson, D.D., van Dokkum, P., Franx, M., Illingworth, G.D. & Magee, D. 1999, ApJ , 522, 39.

Tozzi, P. & Norman, C. 2001, ApJ , 546, 63.

Tucker, W., Blanco, P., Rappaport, S., David, L., Fabricant, D., Falco, E.E., Forman, W., Dressler, A. & Ramella, M. 1998, ApJ , 496, L5.

Viana, P.T.P., & Liddle 1996, MNRAS , 281, 323.

Viana, P.T.P., & Liddle 1999, MNRAS 303, 535.

Vikhlinin, A., McNamara, B.R., Forman, W., Jones, C., Quintana, H. & Hornstrup, A. 1998, ApJ , 503, 77.

Voit, G.M., Evrard, A.E. & Bryan, G.L. 2001, ApJ , 548, L123.

White, D.A. 2000, MNRAS, 312, 663.

White, M. 2000, A&A , 367, 27.

White, S.D.M., Efstathiou, G. & Frenk, C.S. 1993, MNRAS , 262, 1023.

White, S.D.M., Navarro, J.F., Evrard, A.E. & Frenk, C.S. 1993, Nature, 366, 429.

Willick, J.A., Thompson, K.L., Mathiesen, B.F., Perlmutter, S., Knop, R.A. & Hill, G.J. 2001, PASP, 113, 658.

Wilson, G., Kaiser, N. & Luppino, G.A. 2001, ApJ , in press, astro-ph/0102396.

Wu, X.-P., Xue, Y.-J. & Fang, L.-Z. 1999, ApJ , 524, 22.

Yoshida, N., Colberg, J., White, S.D.M., Evrard, A.E., MacFarland, T.J., Couchman, H.M.P., Jenkins, A.R., Frenk, C.S., Pearce, F.R., Efstathiou, G., Peacock, J.A. & Thomas, P.A. 2001, MNRAS , in press, astro-ph/0011212.

Yoshikawa, K., Jing, Y.P., Suto, Y. 2000, ApJ , 535, 593.

Zaritsky, D., Nelson, A.E., Dalcanton, J.J. & Gonzalez, A.H. 1997, ApJ , 480, L91.

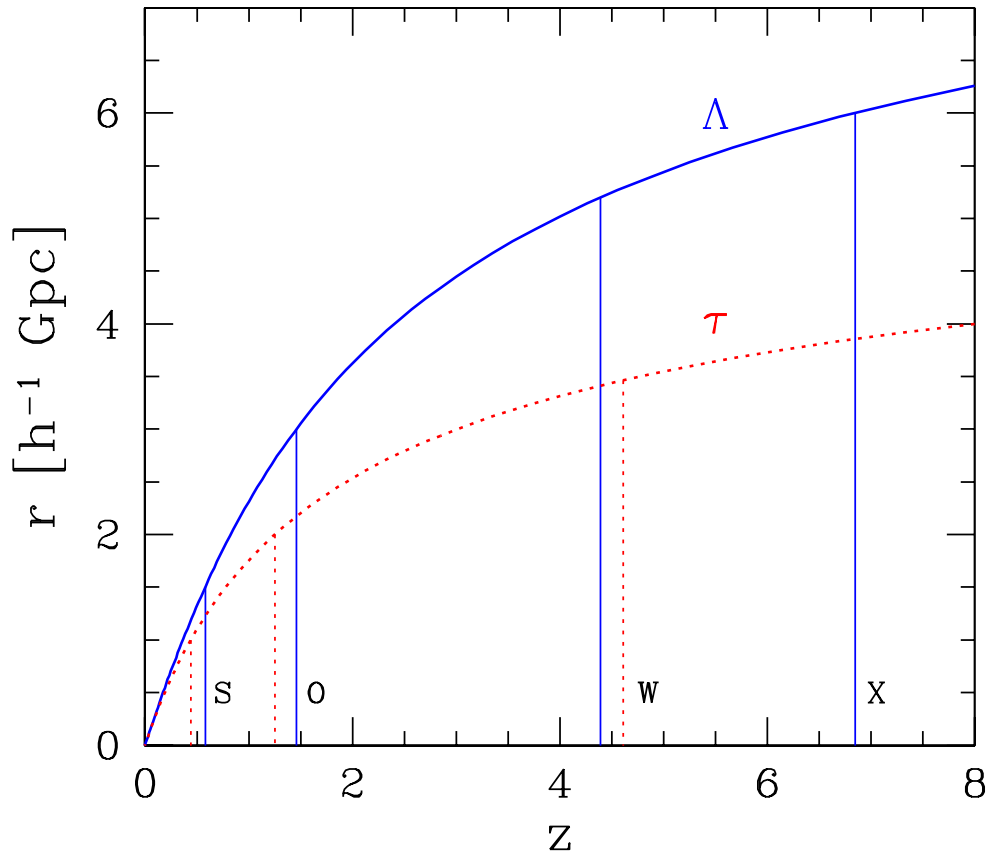


FIG. 1.— Comoving distance as a function of redshift for  $\Lambda$ CDM (solid) and  $\tau$ CDM (dashed). Vertical lines indicate redshift limits of the spherical (S), octant (O), deep wedge (W) and extended wedge (X) surveys (Table 2).

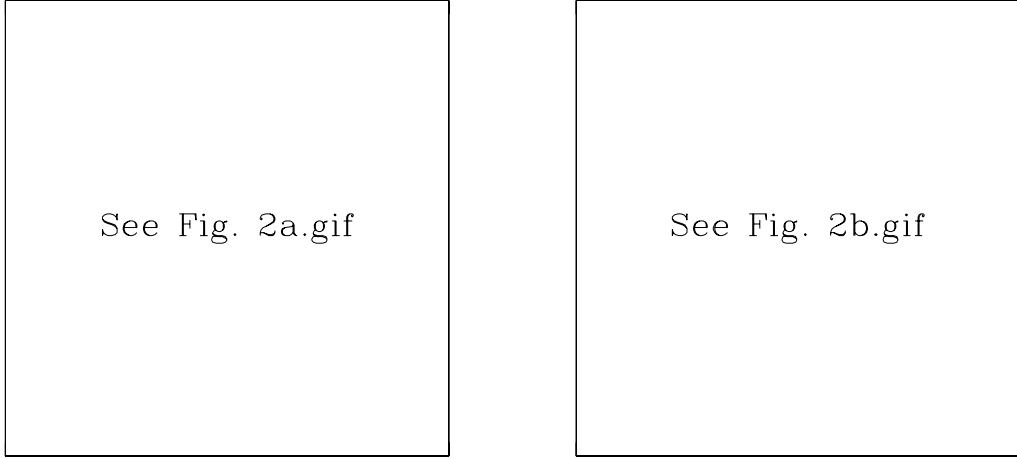


FIG. 2.— Maps of the dark matter density in slices through the deep octant surveys in (a)  $\tau$ CDM and (b)  $\Lambda$ CDM world models. Survey origins are at the vertices (O), and color represents mass density relative to the mean ranging from 0.05 (black) to 50 (white) on a logarithmic scale. Density is mapped onto a two-dimensional grid using an adaptive (Lagrangian) smoothing kernel with scale  $2 \times 10^{13} h^{-1} M_{\odot}$ . For each model, two representations of a  $45^\circ$  slice extending to  $z = 1.25$  are shown. Horizontal maps display structure in the comoving metric while the vertical maps display the same comoving region, reflected about the diagonal, in redshift space. Positions of clusters at the intersection of filaments are evident in redshift space through the radial distortions arising from their internal velocity dispersions (so-called ‘fingers of God’). The inset of the  $\tau$ CDM image shows the relation between comoving distance  $r$  and redshift  $z$  over the range mapped by the images. The inset of the  $\Lambda$ CDM image shows a close-up of the particle distribution around the largest cluster of the  $\Lambda$ CDM octant surveys, located at  $z = 1.04$ . Particles colored white lie within a sphere of physical radius  $1.5 h^{-1}$  Mpc that encompasses a mean density 200 times the critical value.

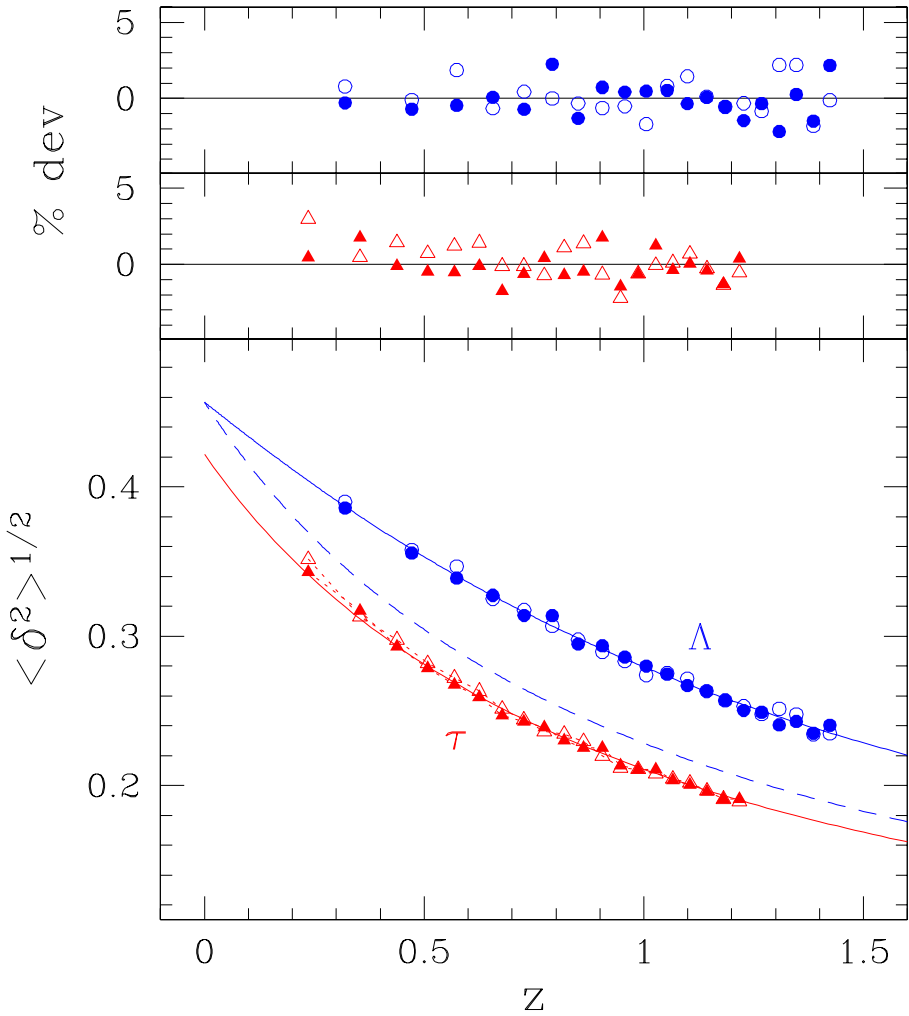


FIG. 3.— Redshift evolution of the *rms* amplitude of density fluctuations  $\langle \delta^2 \rangle^{1/2}$  in top-hat spheres containing, on average, a mass of  $2.2 \times 10^{15} h^{-1} M_\odot$  (1000 particles). Points are octant survey measurements (filled, PO; open, NO) from the  $\Lambda$ CDM (circles) and  $\tau$ CDM (triangles) simulations, obtained by randomly sampling twenty radial shells of equal comoving volume and plotted at the volume-weighted redshift of each shell. Solid lines are predictions from linear theory based on the input fluctuation spectra. The upper panel demonstrates agreement with linear theory at the  $\sim 1\%$  level, except for the non-linear departure of  $\tau$ CDM fluctuations at late times. The dashed line in the lower panel shows the evolution that  $\Lambda$ CDM fluctuations would have if they followed the  $\tau$ CDM linear growth evolution.

see fig4.gif

FIG. 4.— Redshift-space structure in  $75,000 \text{ km s}^{-1}$  wide regions centered at  $z=1.1$  in  $\tau\text{CDM}$  (left) and  $\Lambda\text{CDM}$  (right). The grey-scale shows only overdense material  $\delta > 0$ . The  $\Lambda\text{CDM}$  image includes the most massive cluster in the octant surveys at  $z=1.04$ , visible as the long streak at the lower right. The regions shown lie just interior to the vertical edges of the redshift-space maps of Figure 2.

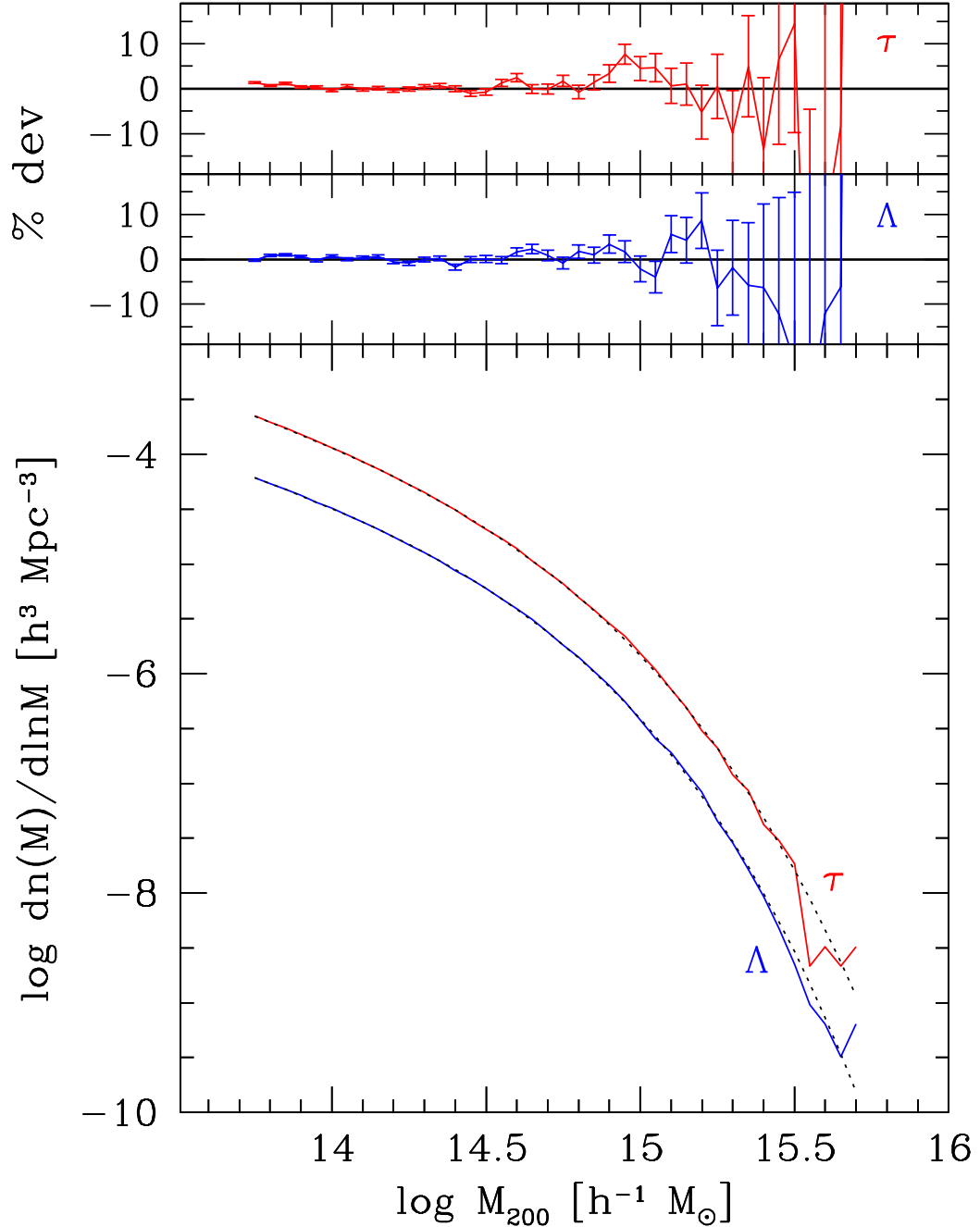


FIG. 5.— The lower panel shows critical SO(200) mass functions derived from the  $z=0$  HV cluster catalogs (solid lines) along with fits to the Jenkins' mass function, equation (9), using parameters listed in Table 4 (dotted lines). Upper panels show the percent deviation in number density between the HV data and the fits. Error bars are based on Poisson statistics in each mass bin.

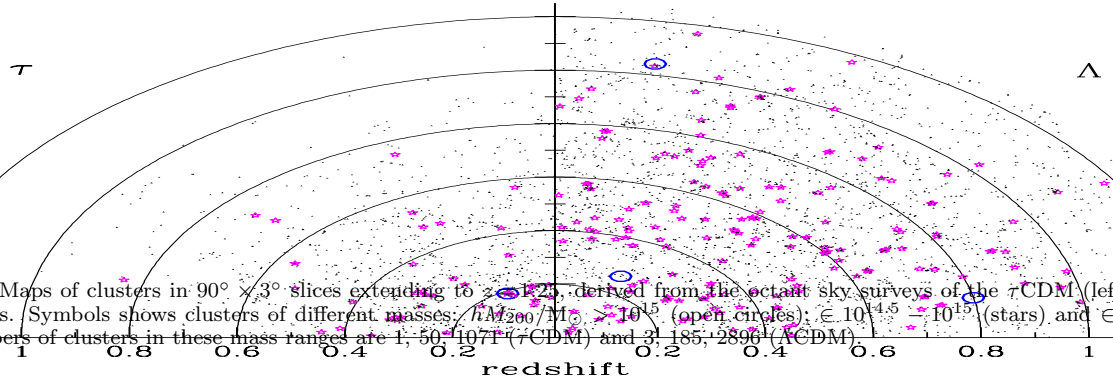


FIG. 6.— Maps of clusters in  $90^\circ \times 3^\circ$  slices extending to  $z = 1.25$ , derived from the octant sky surveys of the  $\tau$ CDM (left) and  $\Lambda$ CDM (right) models. Symbols shows clusters of different masses:  $hM_{200}/M_\odot > 10^{15}$  (open circles);  $\in 10^{14.5} - 10^{15}$  (stars) and  $\in 10^{14} - 10^{14.5}$  (dots). Numbers of clusters in these mass ranges are 1,501,1071 ( $\tau$ CDM) and 31,185,2890 ( $\Lambda$ CDM).

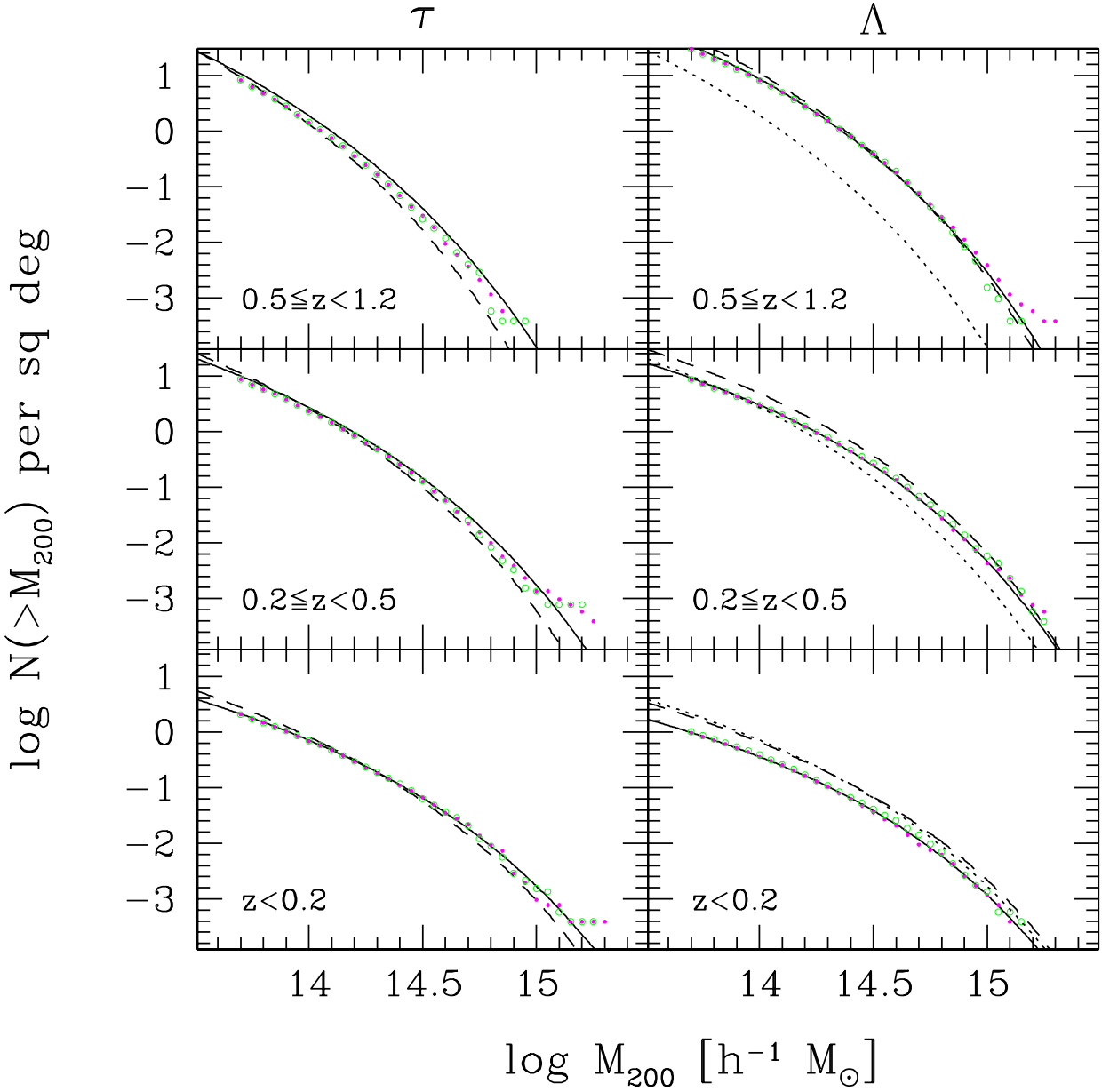


FIG. 7.— Cumulative sky counts of clusters as a function of mass for low, intermediate and high redshift intervals (bottom to top) for  $\tau$ CDM (left) and  $\Lambda$ CDM (right). Smooth solid lines in each panel give the expectations from integrating the Jenkins mass function, equation (9), over the appropriate volumes. Points show counts from the PO (filled circles) and NO (open) octant surveys. Dashed lines are standard Press-Schechter estimates. In the  $\Lambda$ CDM panels, dotted lines display the corresponding JMF expectations for the  $\tau$ CDM cosmology.

$\log N(>M_{200}, >z)$  on whole sky

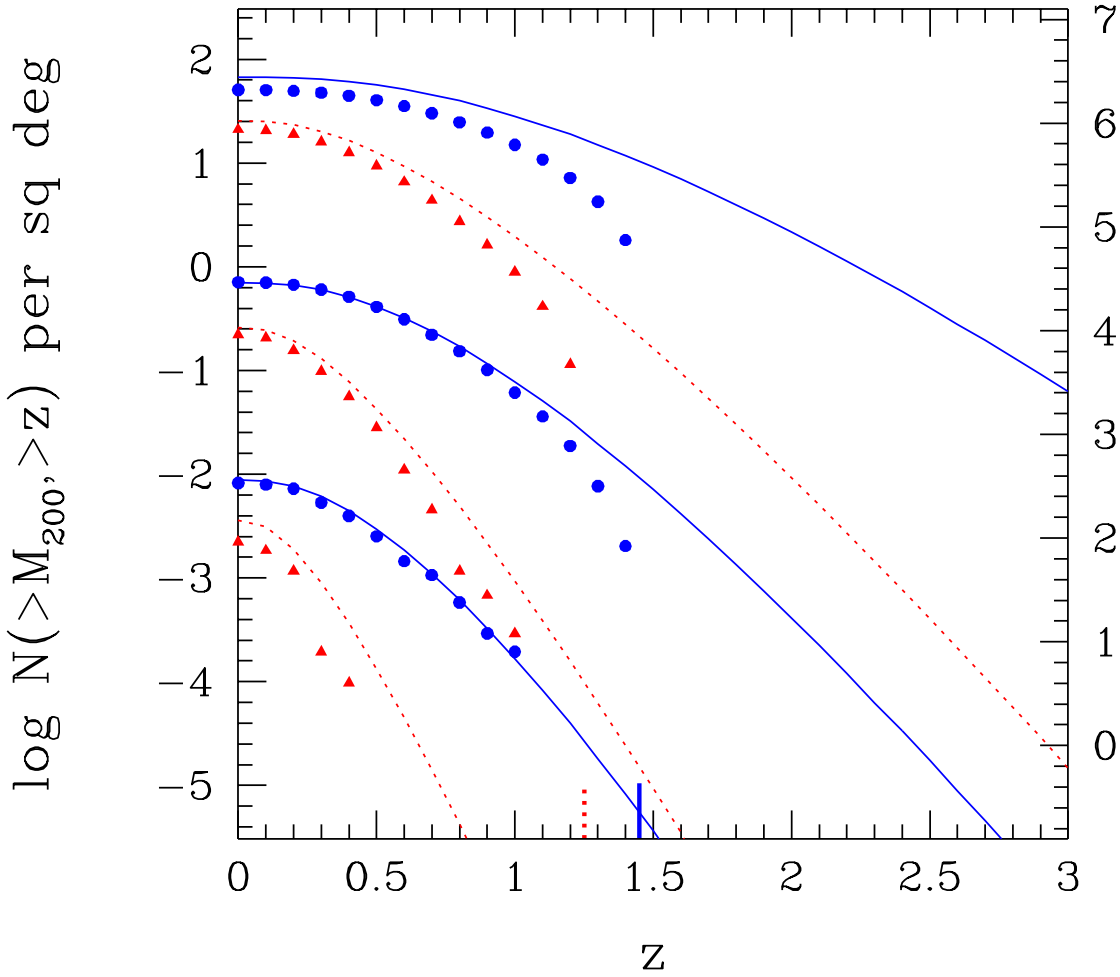


FIG. 8.— Sky surface density of clusters lying at redshift  $z$  or higher in  $\Lambda$ CDM (filled circles, solid lines) and  $\tau$ CDM (filled triangles, dotted lines). Points give numbers derived from the combined octant surveys with masses above  $M_{200} = 5 \times 10^{13}$  (top),  $3 \times 10^{14}$  (middle) and  $10^{15} h^{-1} M_{\odot}$  (bottom). Short vertical lines mark the limiting redshifts of the octant surveys. Lines are expectations at each mass limit derived from integrating the Jenkins mass function.

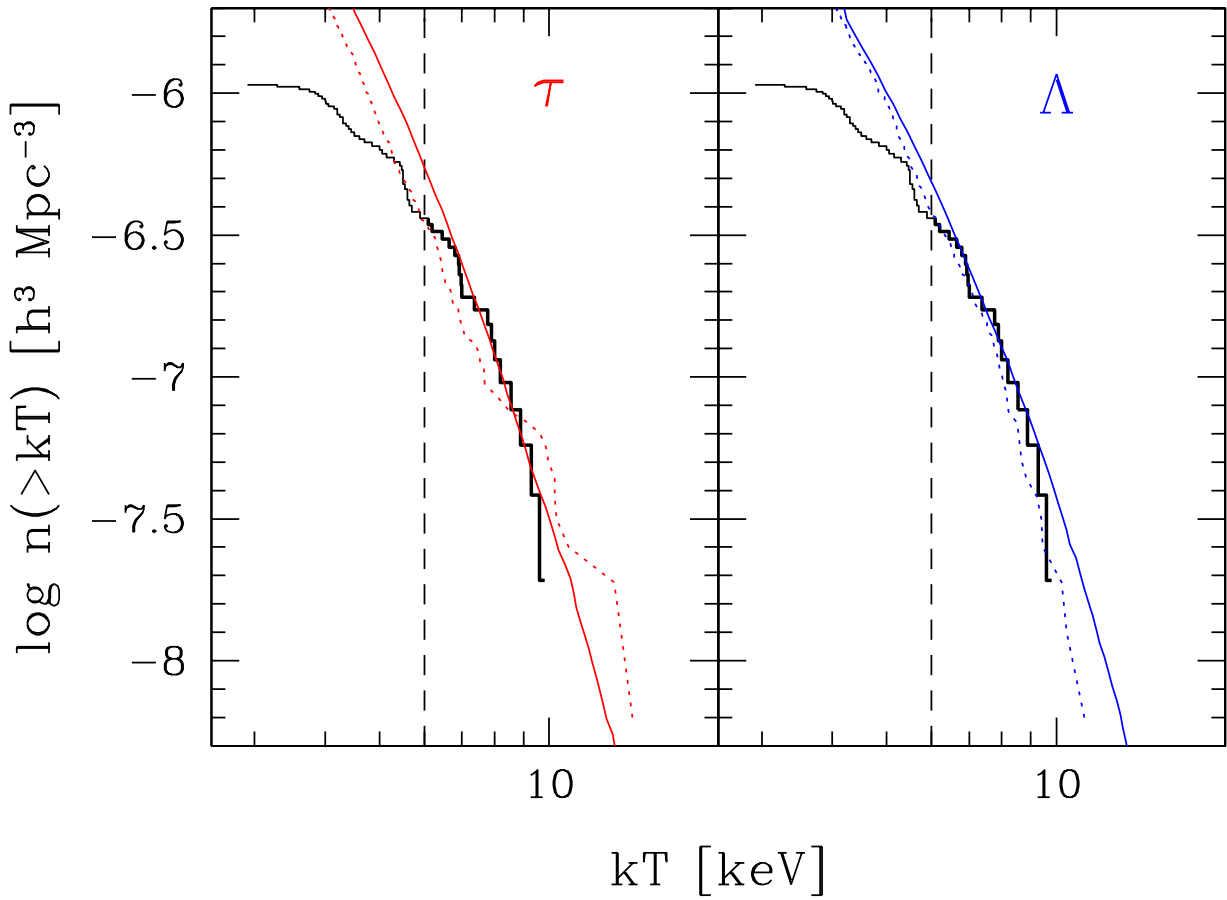


FIG. 9.— Thick lines show the local temperature function of Pierpaoli *et al.* (2001) based largely on data of Markevitch (1998). The HV simulation expectations, using best-fit values  $\beta_\Lambda = 0.92$  and  $\beta_\tau = 1.20$ , are shown from the light-cone (dotted) and  $z = 0$  snapshot (solid) outputs. The former uses clusters within the combined MS and VS surveys lying in the redshift interval  $0.03 < z < 0.09$ . The latter uses the cluster population of the entire computational volume. The vertical dashed line in each panel shows the approximate completeness limit of the observations.

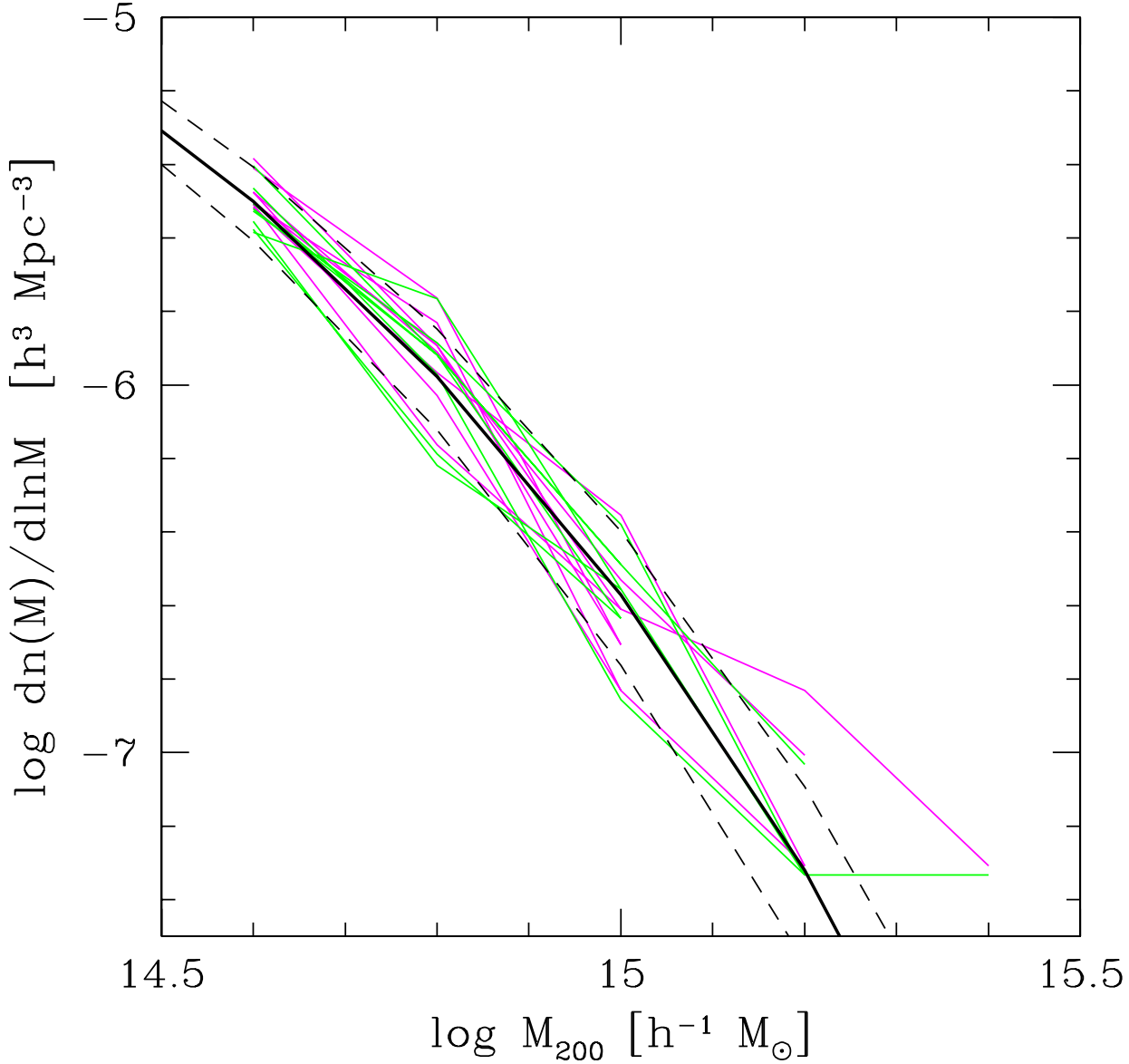


FIG. 10.— Differential mass functions within 16 independent  $\pi/2$  steradian regions extending to  $z = 0.15$ , derived from the MS and VS surveys of the  $\Lambda$ CDM model. The bold line shows expectations of equation (9) using the best fit parameters. Dashed lines show the effect of varying  $\sigma_8$  by  $\pm 5\%$ . The volume of the samples is comparable to that of the local observed sample used to constrain  $\sigma_8$ .

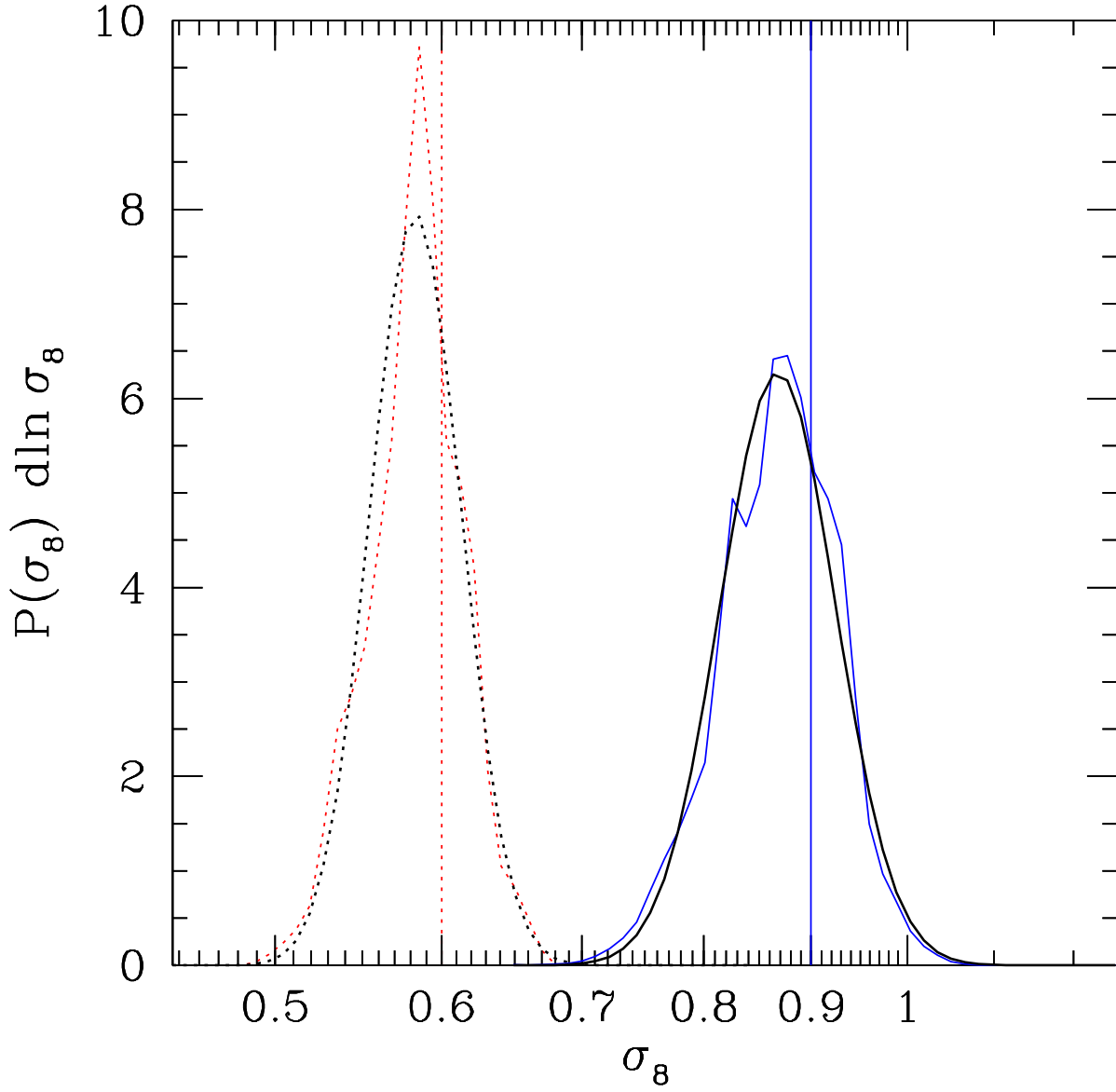


FIG. 11.— Frequency distributions of the maximum likelihood value of  $\sigma_8$  derived from fitting the local mass functions of 1000 ( $\tau$ CDM, dotted) and 4096 ( $\Lambda$ CDM, solid) sub-volumes of the  $z=0$  outputs to mass limits  $6 \times 10^{14}$  ( $\Lambda$ CDM) and  $10^{15} h^{-1} M_\odot$  ( $\tau$ CDM). The chosen mass limits generate an average sample size of  $\sim 30$  within the sub-volumes. The cosmic variance in  $\sigma_8$  is well described by log-normal distributions (smooth curves) of width 0.050 ( $\tau$ CDM) and 0.064 ( $\Lambda$ CDM).

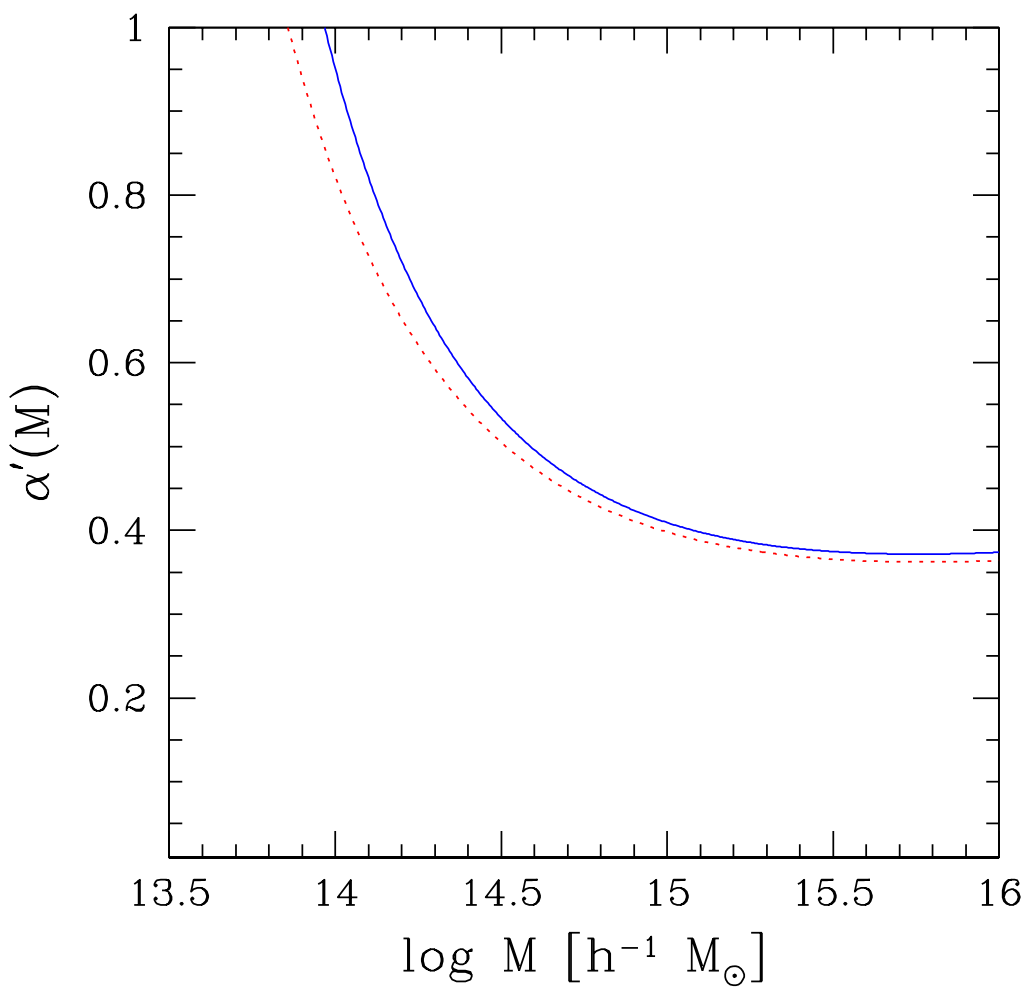


FIG. 12.— The sensitivity  $\alpha'(M)$ , equation (12), for the  $\Lambda$ CDM (solid) and  $\tau$ CDM (dotted) models.

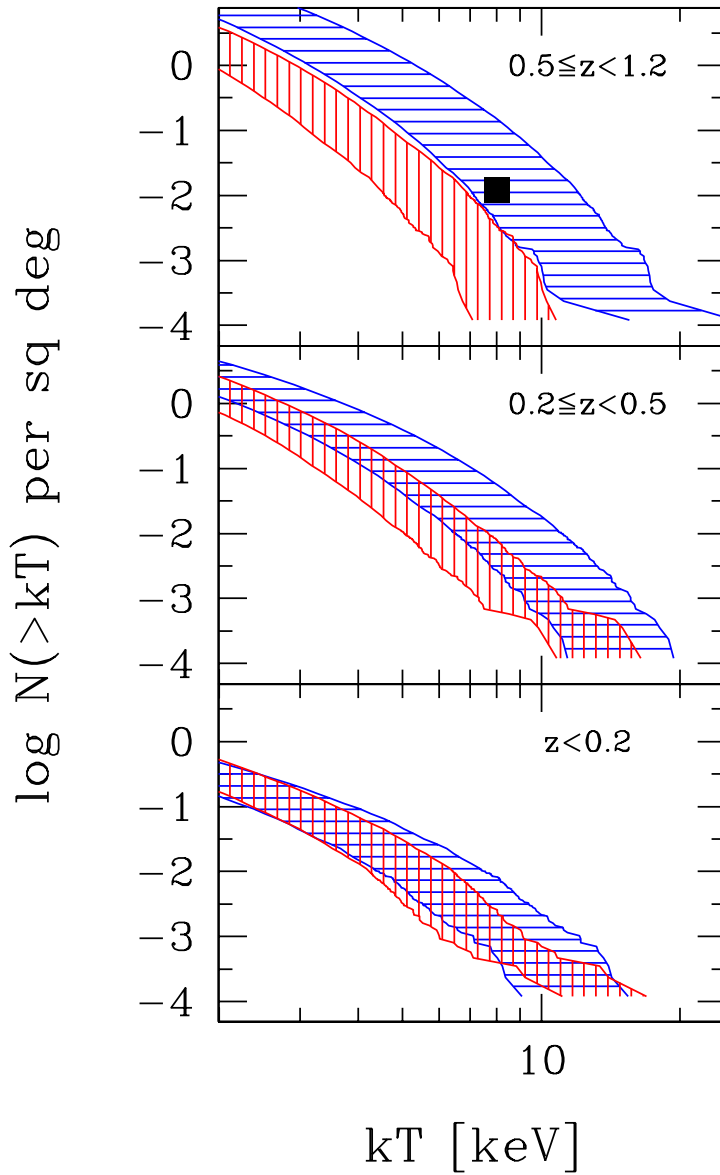


FIG. 13.— The range of cumulative sky surface densities of clusters as a function of temperature in three redshift intervals for the  $\Lambda$ CDM (horizontal hatched) and  $\tau$ CDM (vertical) cosmologies. The range is determined from the combined octant survey counts by varying  $\beta$  within its overall 5 to 95% confidence range. The solid square denotes the EMSS observational result for clusters hotter than 8 keV at  $z > 0.5$ .

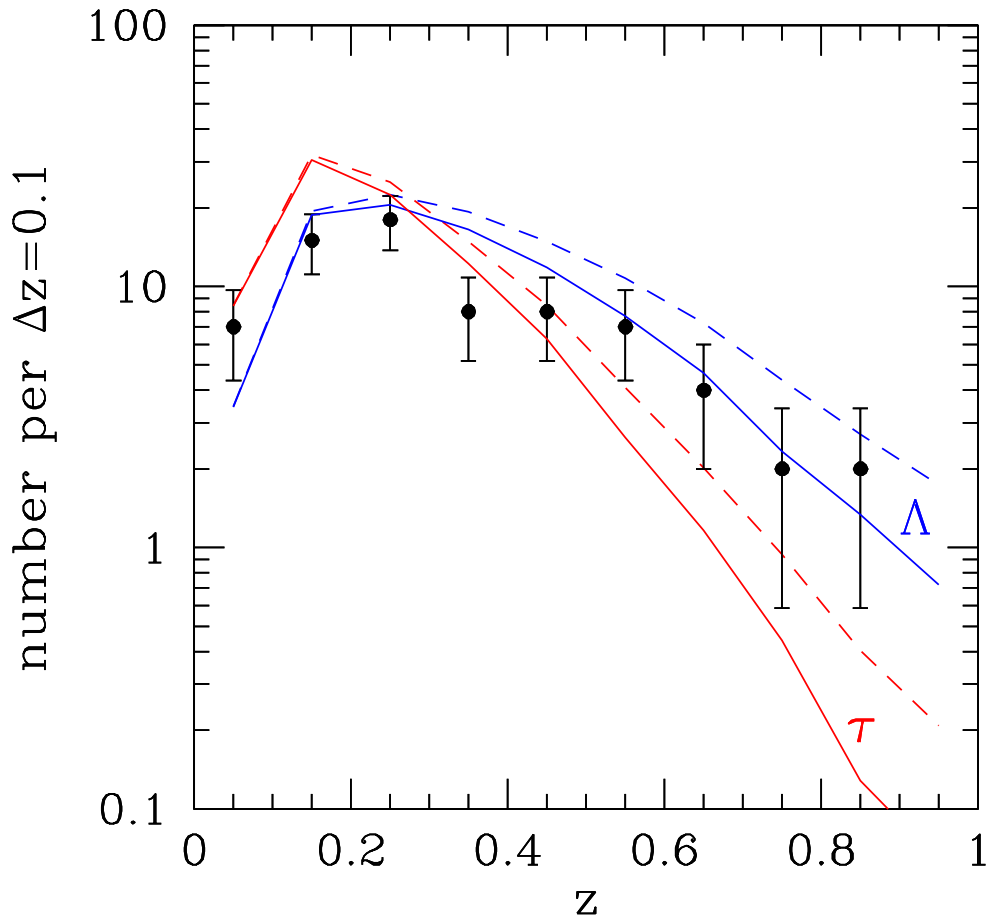


FIG. 14.— Points show the redshift distribution of the X-ray flux-limited RDCS survey (Rosati *et al.* 1998; Borgani *et al.* 1999b), with Poissonian errors. Solid lines show expectations for a 33 sq deg survey derived from the combined octant surveys by assuming constant  $\beta$  and a non-evolving  $L_X-T$  relation. Dashed lines show plausible confusion effects of cooling flows and AGN contamination on the X-ray-selection (see text for details).

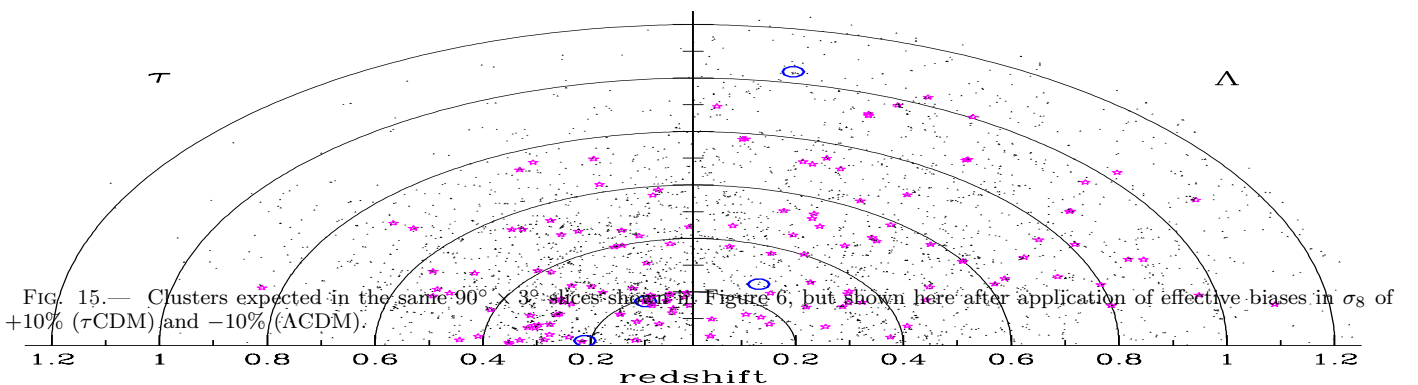


FIG. 15.— Clusters expected in the same  $90^\circ \times 3^\circ$  slices shown in Figure 6, but shown here after application of effective biases in  $\sigma_8$  of  $+10\%$  ( $\tau$ CDM) and  $-10\%$  ( $\Lambda$ CDM).

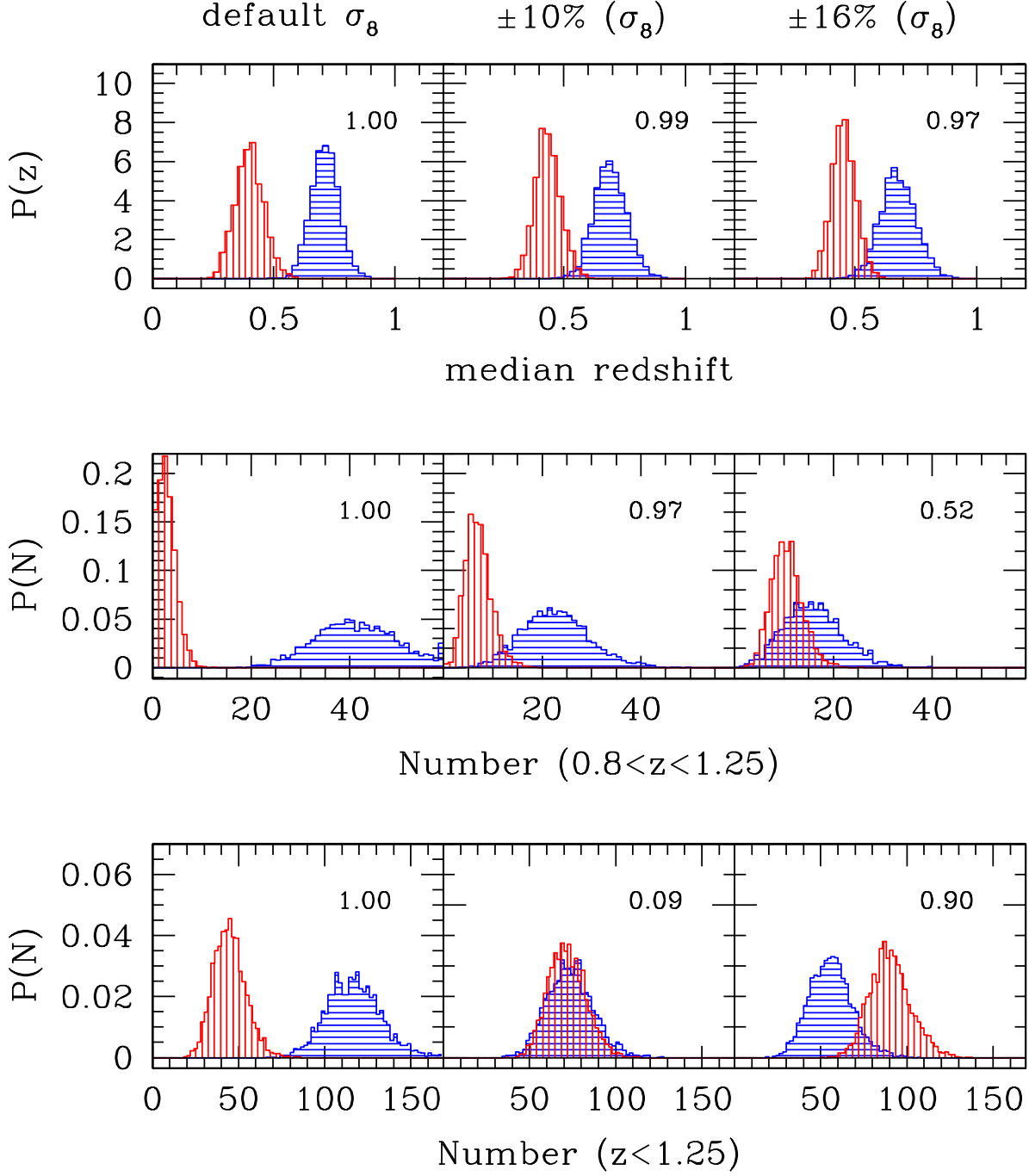


FIG. 16.— The influence of varying  $\sigma_8$  on the population of clusters more massive than  $10^{14} h^{-1} M_\odot$  expected in 10 sq deg survey fields. Columns (left to right) show probability distributions at the default  $\sigma_8$  values,  $(+/-)10\%$  and  $(+/-)16\%$  variation (+ for  $\tau$ CDM/- for  $\Lambda$ CDM) for the counts at redshifts  $z < 1.25$  (bottom row), counts in the high redshift interval  $0.8 < z < 1.25$  (middle) and the median cluster redshift (top). Vertical hatched distributions are  $\tau$ CDM, horizontal are  $\Lambda$ CDM. Numbers in each panel give the power statistic described in the text. The distributions are generated by sampling 10 sq deg fields around 3000 randomly chosen pointings in the combined octant surveys of each model. Shifts in mass and number, equation (15) are used to effectively vary  $\sigma_8$  in the cluster catalogs.

$\log N(>M_{200}, >z)$  on whole sky

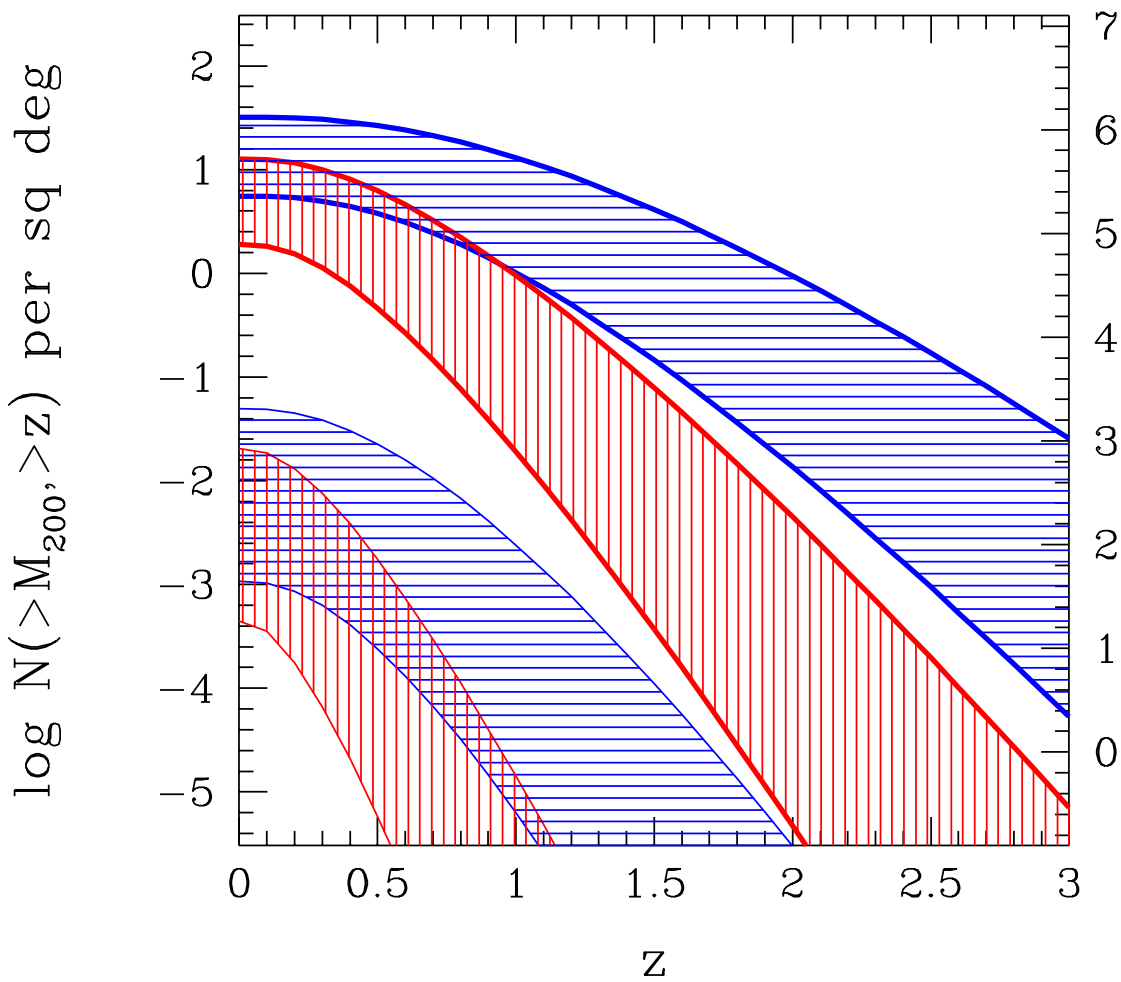


FIG. 17.— Ranges of cluster counts versus redshift in the  $\Lambda$ CDM (horizontal hatch) and  $\tau$ CDM (vertical) models expected above  $10^{14}$  (upper, bold border) and  $10^{15} h^{-1} M_\odot$  (lower, light border). The ranges are determined by integrating the Jenkins mass function using the 5 and 95 percent confidence values of  $\sigma_8$  for each model.

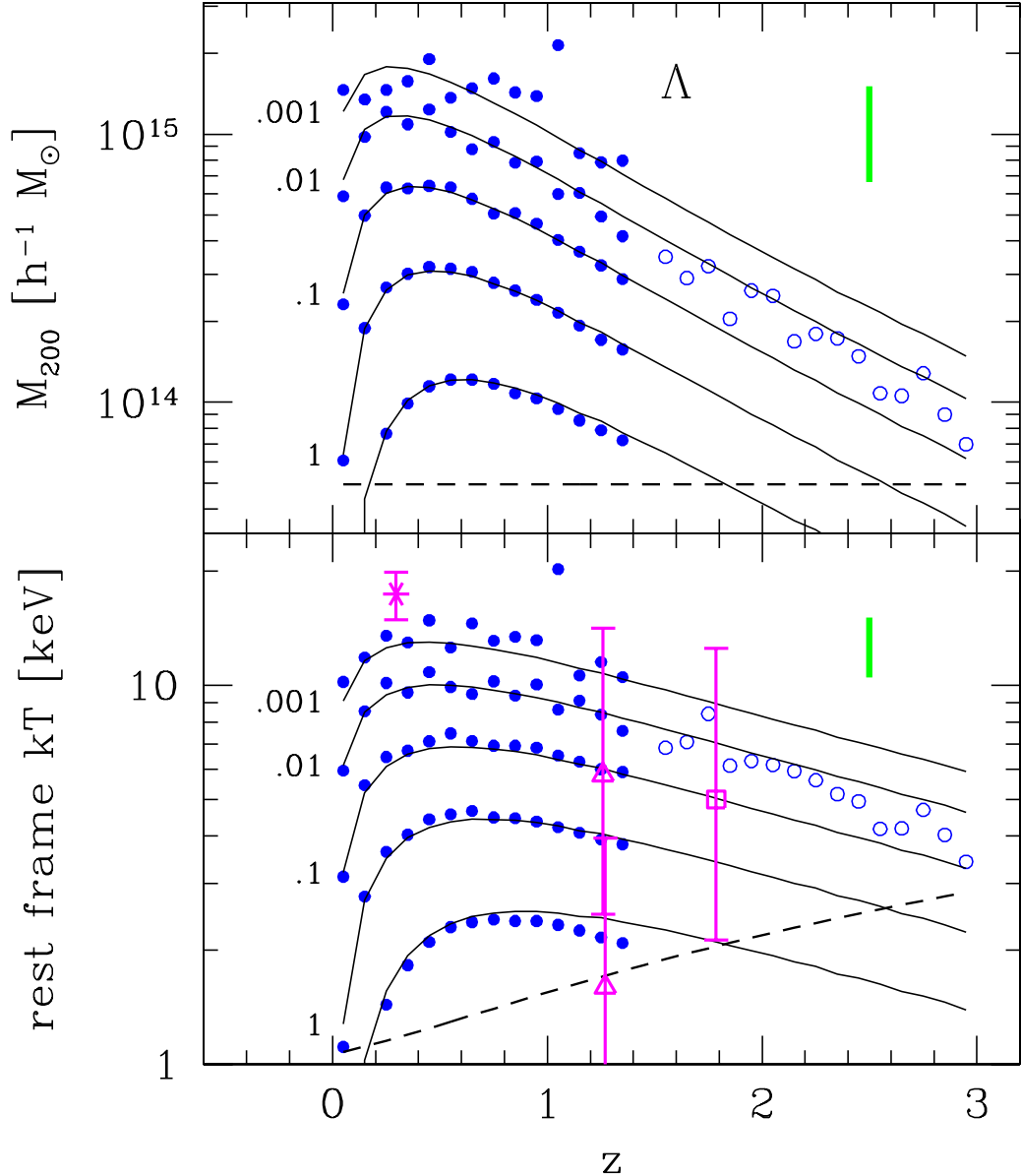
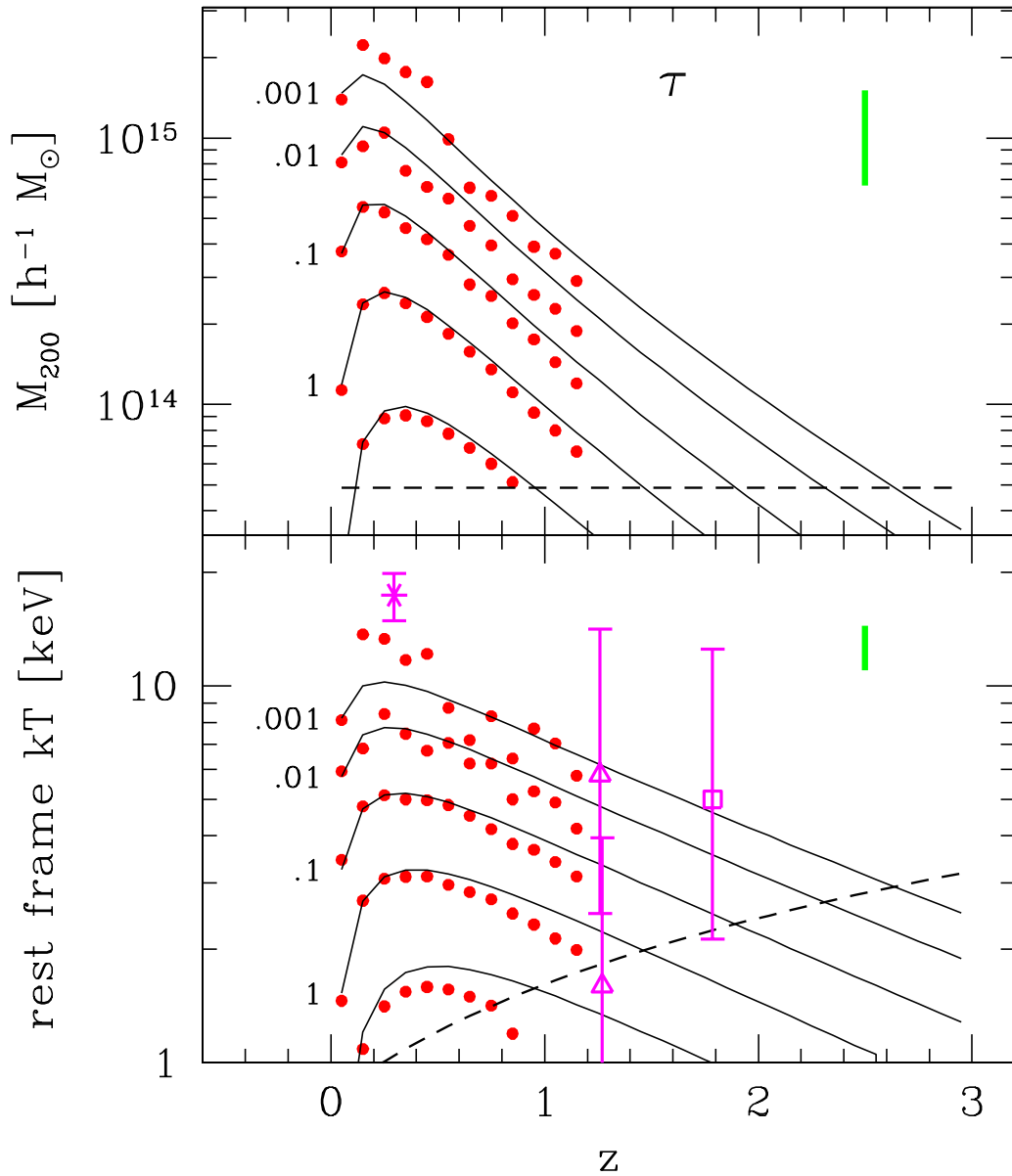


FIG. 18.— Sky surface density characteristic mass (upper) and temperature (lower) in the  $\Lambda$ CDM model. Points are based on the 10,000 sq deg combined octant surveys (filled circles) and the 1000 square degree extension (open circles) and show the mass and temperature above which the cluster sky surface density in the redshift interval  $z - 0.05$  to  $z + 0.05$  exceeds values 0.001, 0.01, 0.1, 1 and 10 per sq deg per unit redshift. Clusters at the lowest density shown are the most massive or hottest cluster in that redshift interval within the combined octant surveys. Note the exceptional nature of the ‘monster’ cluster at  $z = 1.04$ . Solid lines are expectations based on the Jenkins mass function and the virial theorem, as described in the text. The vertical bars in each panel denote the 90% confidence range of uncertainty in the absolute calibration of mass and temperature scales. Open triangles and squares plot temperature and redshift extremes of the known X-ray cluster population: RX J0849+4452 at  $z = 1.26$  and RX J0848+4453 at  $z = 1.27$  (Stanford *et al.* 2000, triangles); 3C294 at  $z = 1.786$  (Fabian *et al.* 2001, square) and 1E 0657-56 at  $z = 0.296$  (Tucker *et al.* 2001, asterisk). Dashed lines correspond to a mass limit of 22 simulation particles (upper panel) and the temperature at that mass scale (lower).

FIG. 19.— Same as Figure 18, but for the  $\tau$ CDM model.

## APPENDIX

## A. CLUSTER FINDING DETAILS AND COMPLETENESS CHECKS

The cluster finding algorithm that produced the catalogs in this paper begins by generating a density estimate for each particle using the distance to its eighth nearest neighbor (Casertano & Hut 1985), equivalent to Lagrangian filtering on a mass scale  $2 \times 10^{13} h^{-1} M_\odot$ . Sorting density values in decreasing order provides a list of potential sites for cluster centers. The list is pruned by eliminating particles whose densities lie below the threshold  $\Delta\rho_c(z)$ . Beginning with the first member of the sorted list, a sphere of radius  $r_\Delta$  enclosing mass  $M_\Delta$  is defined about that particle so that the enclosed density  $\rho \equiv 3M_\Delta/4\pi r_\Delta^3 = \Delta\rho_c(z)$ . Particles lying within this sphere are recorded as members of this group and are removed from the list of potential cluster centers. The process is repeated sequentially, centering on the next available particle in the list ordered by decreasing density, until the list is exhausted. Particles may belong to more than one group, but the center of a given group never lies within the spherical boundary of another group.

In analyzing SO(180) and mean SO(324) populations of the  $\tau$ CDM and  $\Lambda$ CDM models, respectively, J01 noted a problem of incompleteness in the SO cluster finding algorithm at particle counts  $\lesssim 100$ . Resolution tests in J01 indicated that space densities of groups comprised of 20 particles could be underestimated by  $\sim 30\%$ . We employ here an independent SO algorithm with improved completeness properties at small numbers of particles. Figure A1 compares the SO(180) and mean SO(324) abundance functions (for  $\tau$ CDM and  $\Lambda$ CDM, respectively) at  $z=0$  based on the new algorithm to the fits published in Appendix B of J01.

In the figure, the thick solid line show J01 functional fits while the thin solid and dotted lines show discrete mass functions derived with the algorithm employed here. The dot-dashed line is the discrete  $\tau$ CDM mass function derived by J01 using the previous SO algorithm. The top panel shows the percent deviation between the discrete sample measurements and the fit expectations.

For the  $\tau$ CDM case, both the old and new algorithms compare well against each other and against the fit above  $\sim 10^{15} h^{-1} M_\odot$ . At lower masses, the J01 algorithm displays an increasing underestimate in number density with respect to the fit, approaching a 30% underestimate at the mass limit  $5 \times 10^{13} h^{-1} M_\odot$  used in this work. The new SO algorithm (dotted) displays a similar qualitative trend, but the underestimate is reduced to  $\lesssim 10\%$  in amplitude. A similar trend is seen for the new algorithm in the  $\Lambda$ CDM case where the number density lies  $\sim 12\%$  lower than the J01 fit expectations. This analysis indicates that the amplitude  $A$  derived from fitting the space density to the Jenkins form, to equation (9), may be biased low by  $\sim 10\%$  at masses below  $\sim 10^{15} h^{-1} M_\odot$ .

A further check of resolution effects is made by directly comparing the HV mass function to one derived from smaller volumes with improved mass resolution. We do this for SO(200) clusters in the  $\Lambda$ CDM model at  $z=0$ , using data from the  $256^3$  particle simulation of a  $239.5 h^{-1}$  Mpc region from Jenkins *et al.* (1998). The new SO(200) algorithm is used to identify clusters in the same manner as done in the HV simulation. The cosmological parameters for the models are the same, except for a slight difference in the power spectrum used to generate the initial conditions, whereas the particle mass in the  $256^3$  particle simulation is a factor 32 times smaller than that used in the HV computations.

Figure A2 shows the cumulative number of clusters found in the  $256^3$  particle simulation (dotted line) along with the number expected based on the  $z=0$  HV population (solid). Vertical bars on the HV results show the range in number derived from dividing the HV volume into 1728 independent cubes of side  $250 h^{-1}$  Mpc and rescaling the counts in each cube to a  $(239.5 h^{-1}$  Mpc) $^3$  volume. The inset shows the correlation between counts above  $5 \times 10^{13}$  and  $3 \times 10^{14} h^{-1} M_\odot$  within the subvolumes. The small-volume simulation result is inconsistent with the HV distribution; the count distribution shows agreement at the 98% level at  $3 \times 10^{14} h^{-1} M_\odot$  but the  $5 \times 10^{13}$  count is  $\sim 0.5\%$  higher than the maximum of the HV distribution and  $\sim 20\%$  above the mean.

These findings, along with the slight discrepancy in predicted versus measured counts in the  $\tau$ CDM octant surveys (Figure 7) lead to a conservative estimate of the systematic theoretical uncertainty in the number density of clusters above  $10^{14} h^{-1} M_\odot$  to be 20%. Future studies, in particular those which cross-calibrate results for a particular cosmology modeled by different simulation teams, are needed to better assess the overall accuracy of this model of the mass function.

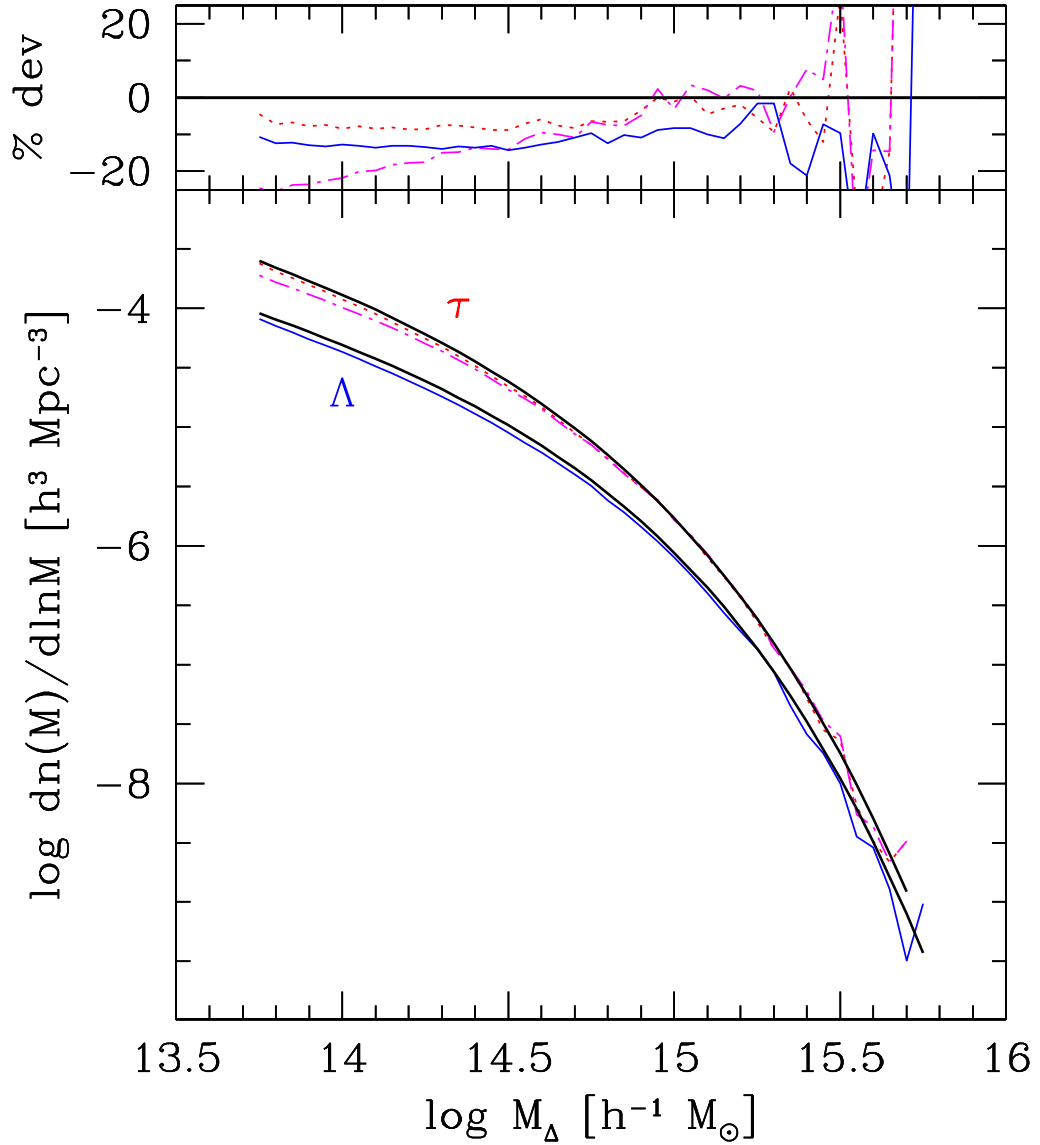


FIG. A1.— Differential SO mass functions at  $z=0$  are compared to the fits published in J01. In the lower panel, thick lines are the J01 expectations (from their Appendix B) for  $\tau$ CDM at  $\Delta = 180$  (upper curve) and  $\Lambda$ CDM at mean  $\Delta = 324$  (critical  $\Delta = 97.2$ , lower curve). The  $\Lambda$ CDM simulation data are shown by the slightly jagged solid curve. Two simulation results are shown for  $\tau$ CDM—the dot-dashed line reflects the SO algorithm used by J01 and the dotted line shows results of the algorithm used in this work. The upper panel displays the percent deviation in number density between the HV simulation data and the J01 model fits.

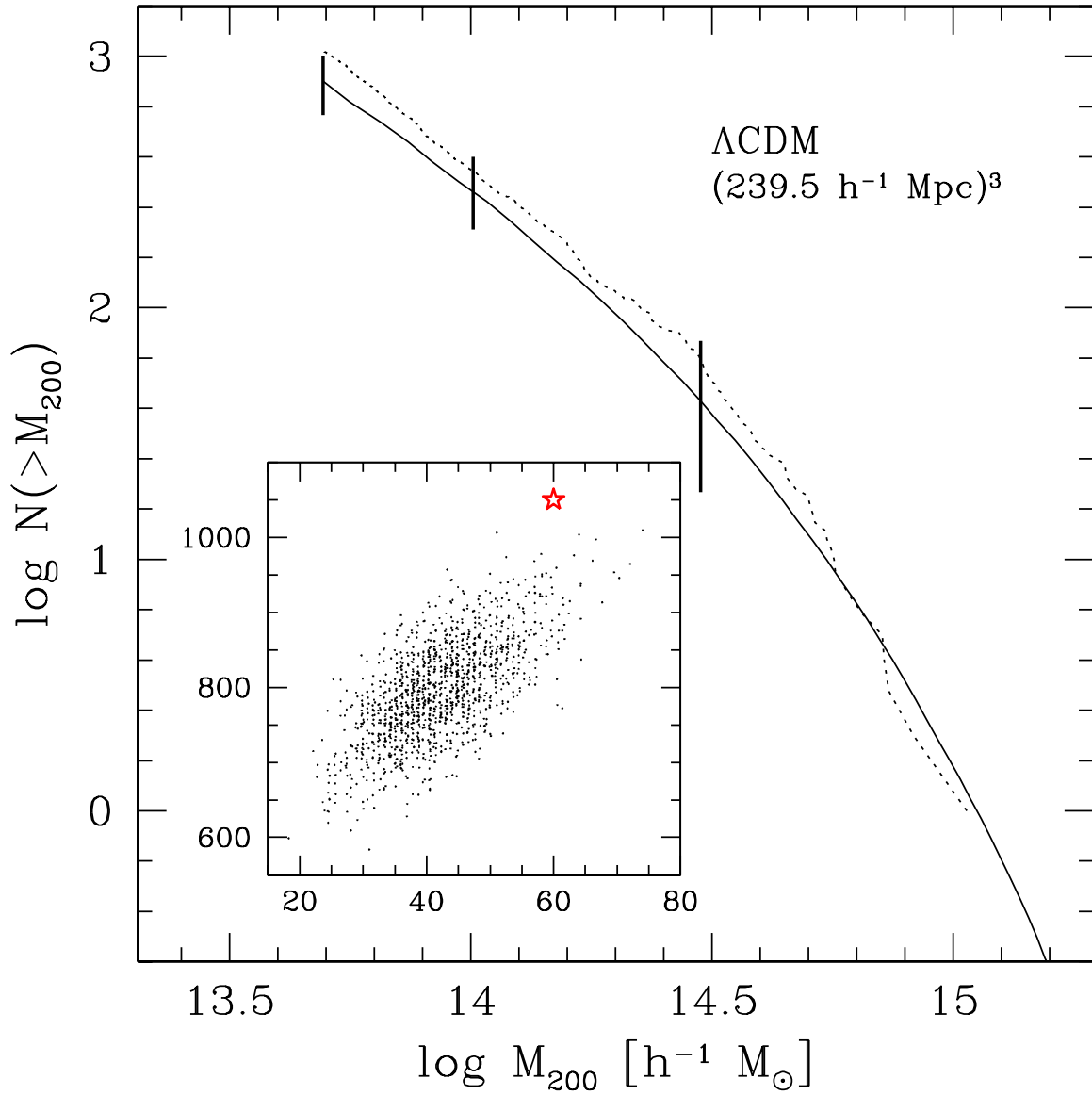


FIG. A2.— The cumulative number of clusters within the volume indicated, scaled from the full  $z=0$  HV simulation (solid line) and from a single realization of a  $(239.5 h^{-1} \text{ Mpc})^3$  volume (Jenkins *et al.* 1998; dotted line) for the  $\Lambda$ CDM cosmology. Vertical lines show the entire range of counts above masses  $5 \times 10^{13}$ ,  $10^{14}$  and  $3 \times 10^{14} h^{-1} M_\odot$  derived from subsampling 1728 cubic sub-volumes of side  $250 h^{-1} \text{ Mpc}$  within the HV realization and scaling to  $239.5 h^{-1} \text{ Mpc}$ . The inset plots the correlation of counts above  $3 \times 10^{14}$  ( $x$ -axis) and  $5 \times 10^{13}$  ( $y$ -axis) derived from the sub-volumes. The star indicates the Jenkins *et al.* (1998) values.

## B. MASS SCALE RENORMALIZATION

The mass scale of clusters at fixed space density is uncertain, both theoretically and empirically, for reasons discussed in the opening section. The lack of a uniquely defined scale motivates a model that would transform the JMF fit parameters derived in §3.3 to values appropriate for a redefined mass scale. As an example, we develop here a model to estimate the SO mass function fit parameters for threshold values  $\Delta \neq 200$ . The method is similar to that used in §5.2 to effectively vary  $\sigma_8$  within the discrete cluster samples.

We have chosen a convention in which a spherical density threshold  $\Delta = 200$  defines cluster masses  $M$ . A choice  $\Delta \neq 200$  would lead to a new mass  $M'$  for each cluster related to the original by some factor

$$M' = M e^\mu. \quad (\text{B1})$$

The space density of a set of *disjoint* clusters is fixed, implying

$$n(M') d \ln M' = n(M) d \ln M. \quad (\text{B2})$$

This condition, with equation (B1), when used with the space density, equation (9), leads to a relation between JMF parameters

$$\begin{aligned} A' &= A e^\mu \\ B' &= B - \alpha_{\text{eff}}(M) \mu \end{aligned} \quad (\text{B3})$$

to first order in  $\mu$ .

The factor  $\mu$  can be calculated from an assumed mass profile. We use the form introduced by Navarro *et al.* (1996; hereafter NFW),

$$M(x) = \frac{800\pi}{3} \rho_c r_{200}^3 \left[ \frac{\ln(1+cx) - cx/(1+cx)}{\ln(1+c) - c/(1+c)} \right] \quad (\text{B4})$$

where  $x = r/r_{200}$  is a scaled radius and  $c$  is a concentration parameter. N-body simulations suggest  $c \simeq 5$  at masses near  $10^{15} h^{-1}$  Mpc for the cosmologies studied here (NFW, Frenk *et al.* 1999; Jing 2000; Bullock *et al.* 2001).

Figure B1 shows the results of applying equation (B3) to critical contrasts  $\Delta = 97.2$  and 500 for the  $\Lambda$ CDM model, assuming  $c = 5$ . The logarithmic shifts in mass scale are  $\mu = 0.093$  and  $-0.141$ , respectively. The agreement between the predicted and measured values is quite good. At  $\Delta = 97.2$  (equivalent to the mean contrast of 324 used by J01), the bin-averaged mean fractional error and dispersion (for bins with 10% or less Poisson uncertainty) are only 4.1% and 3.8%. At  $\Delta = 500$ , the mean is  $-14.5\%$  and dispersion 4.9%.

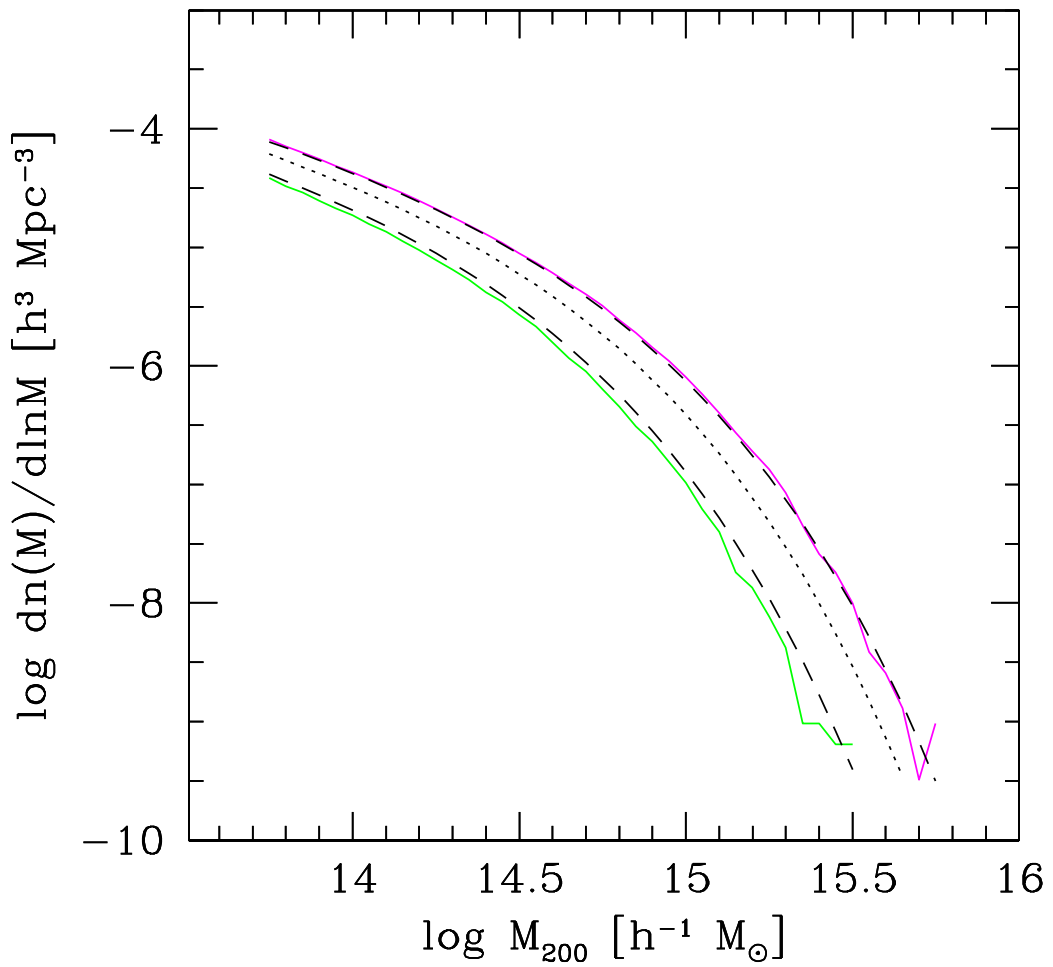


FIG. B1.— The critical SO(500) and SO(97.2) mass functions (lower and upper, respectively) at  $z=0$  for  $\Lambda$ CDM. Solid lines are measured from the HV simulation while dashed lines are predictions based on rescaling the SO(200) JMF fit (dotted line), assuming an NFW profile with concentration parameter  $c=5$ .

This figure "fig2a.gif" is available in "gif" format from:

<http://arxiv.org/ps/astro-ph/0110246v1>

This figure "fig2b.gif" is available in "gif" format from:

<http://arxiv.org/ps/astro-ph/0110246v1>

This figure "fig4.gif" is available in "gif" format from:

<http://arxiv.org/ps/astro-ph/0110246v1>